1992ApJ...387..591J

THE ASTROPHYSICAL JOURNAL, 387:591–611, 1992 March 10
© 1992. The American Astronomical Society. All rights reserved. Printed in U.S.A.

THE SHARPLESS 187 GAS COMPLEX: A MULTIFREQUENCY STUDY

G. JONCAS
Département de Physique and Observatoire du mont Mégantic, Université Laval, Québec, Québec, Canada G1K 7P4
D. DURAND
Dominion Astrophysical Observatory, National Research Council of Canada, 5071 W. Saanich Road, Victoria, B.C., Canada V8X 4M6
AND
R. S. ROGER
Dominion Radio Astrophysical Observatory, National Research Council of Canada, Box 248, Penticton, B.C., Canada V2A 6K3
Received 1991 June 20; accepted 1991 September 18

ABSTRACT

We have observed/analyzed the Sh 187 gas complex in the optical (B, V, R photometry and Hα Fabry-Perot interferometry), radio (continuum and H I line at 21 cm, ^{13}CO), and the IR (*IRAS* co-add maps). The Hα profiles were split in two velocity components over part of the H II region. More than one phenomenon may drive the kinematics of the nebula. A kinematical age of about 2×10^5 yr was derived for the H II region. There is little resemblance between the 1.4 GHz radio continuum and optical emission, indicating that Sh 187 is still enshrouded in the parental cloud. The nebula is almost circular with a peak density ($\langle n_{H+He} \rangle$) of 100 cm^{-3} and a total mass of ionized gas of 7 $M_\odot$. A B0 star is needed to produce the adequate number of ionizing photons. The most fascinating result is that the H II region is partially surrounded by an inhomogeneous H I feature ($M = 70\ M_\odot$) with a NW to the SE velocity gradient. The characteristics of the H I feature (density, thickness, mass, and temperature) is concordant with the predicted values of the Roger-Dewdney model of H I dissociation zones. Hence the presence of H I may result from the dissociation of the surrounding molecular material. The molecular cloud covers more than a degree on the sky. However IR emission is detected only in the inner 35′, centered on the H II region. The behavior of the 12 and 25 μm emission is indicative of the presence of very small grains in the object. Using global properties, the dust opacity to the Lyman continuum photons was calculated to be 0.74, leading to a minimum grain size of 0.004 μm. The presence of a maser/bipolar outflow and a few IR point sources indicates that star formation is still going on in the Sh 187 gas complex. Massive stars (earlier than spectral type B0) are absent from the scene.

Subject headings: H II regions — infrared: interstellar continuum — ISM: individual (Sharpless 187) — radio lines: atomic

1. INTRODUCTION

One of the major goals of astronomy is the understanding of star formation. This is a difficult endeavor for both theoreticians and observers. The latter have to deal with massive absorption, the necessity of high spatial and spectral resolution, and the need of multifrequency observing. The use of many spectral domains to fathom star-forming regions comes from the presence of different components and gas states indicating varying physical conditions. These conditions reflect the star-forming activity and the stage of its development.

When studying a star-forming gas complex, we are facing intricate interplays between the stars' radiation field, the gas (either ionized, atomic, or molecular), and dust. Energetic phenomena like stellar winds, Champagne flows, shock waves, dissociation fronts, etc., are always involved. Obtaining an overall picture of the relative importance of these phenomena with respect to the age and characteristics of the star and gas complexes is needed to produce a self-consistent scenario for their evolution. Such a project is underway (Joncas, Kömpe, & De La Noe 1988; Kömpe et al. 1989). We now add the young star-forming region Sh 187 (Sharpless 1959) to our sample of well studied objects.

Sh 187 is a small H II region (diameter about 9′) located in the Orion arm of our Galaxy ($l = 126.°68$, $b = -0.°82$, $d_{kin} = 1$ kpc). On the Palomar Observatory Sky Survey (POSS), the nebula appears as a bright core (diameter about 1′) surrounded by fainter nebulosity. Sh 187 sits on top of a relatively large absorption lane, suggesting the presence of a molecular cloud. Indeed Blair et al. (1975) detected carbon monoxide over a $6' \times 16'$ area near the H II region. The lines were centered at $V_{lsr} = -15$ km s^{-1}.

Felli & Churchwell (1972) detected Sh 187 in their low-resolution (HPBW = 10′) 1.4 GHz survey of galactic H II regions. Because of this resolution the object appeared featureless with a flux density of 1.8 Jy. High-resolution radio continuum observations of the nebula at 1.4 GHz (Israel 1977) revealed the presence of two components. The brightest one (S187A) was mistakenly taken to be the H II region. It is in fact a nonthermal extragalactic radio source (this work, Snell & Bally 1986). S187B is the H II region. Rossano (1977, 1978) made 5 GHz continuum and H109α recombination line observations of Sh 187 (HPBW = 6.′1). From the continuum observations, he determined the exciting star to be a B0.5 ZAMS star. The H109α line was detected at -14.6 ± 0.4 km s^{-1} (V_{lsr}). Assuming Sh 187 to be isothermal and in LTE at the observed frequency, he calculated an electron temperature of 6200 ± 1240 K. Snell & Bally (1986) presented a 1.4 GHz VLA map of Sh 187 taken with the C configuration. The H II region appears as a cavity surrounded by a bright rim. This appearance must be taken with caution since the map was not pro-

© American Astronomical Society • Provided by the NASA Astrophysics Data System

1992ApJ...387..591J

duced from a fully sampled u-v plane. The flux density contribution from the large scale structures ($< 7'$) is missing.

Bally & Lada (1983) detected a high-velocity molecular flow near the core of the molecular cloud while Lo & Burke (1973) and Henkel, Haschick, & Gusten (1986) observed a multi-component H_2O maser at the sample position. The H_2O maser may be variable. Measurements made at the same position in 1987 during the Arcetri survey (Comoretto et al. 1990) did not provide a detection at the 3 σ level (11.3 Jy). Recently a strongly polarized OH maser was detected near the H_2O maser at $V_{lsr} = -11.5$ km s^{-1} (Braz et al. 1990). The HPBW of their instrument prevents us from speculating on the positional coincidence of both masers. These observations suggest that the Sh 187 gas complex is still undergoing star formation.

2. INSTRUMENTATION AND DATA REDUCTION

2.1. *Optical*

The observations were obtained at the f/8 Ritchey-Chretien focus of the Observatoire Astronomique du mont Mégantic 1.6 m telescope. The Université Laval focal reducer was attached to the telescope and used in its imagery and interferometry mode. The instrument is described in detail in Joncas & Roy (1984). Since then the camera lens was changed so that a CCD detector could be used. We now have a f/8 to f/3.5 focal reduction. The CCD is a RCA chip (320 × 512 pixels) with a read noise of 55e. The scale on the CCD is 1.″1 pixel^{-1} (30 μm pixel) giving a 5.′5 × 8.′8 (NS × EW) field of view. The use of a sensitive detector enhances the possibility of finding some Fabry-Perot (F.P.) rings corrupted by ghosts originating from very bright portions of the object (Georgelin 1970). To prevent such an effect, the CCD was off-centered so that the chip covered half the field of view provided by the focal reducer. The other half was masked.

Using the focal reducer as a two-dimensional photometer, BVR photometry of the stars associated with Sh 187 was obtained. Due to the poor transmission of the focal reducer in the short visible wavelengths we did not attempt any observations in the U band. The stellar cluster NGC 7790 was used as a calibrator and was observed at the same air mass. Three frames of 40, 5, and 4 s, respectively, were taken through each filter for NGC 7790. Similarly, exposures of 300, 60, and 40 s were taken of a field centered on Sh 187. Unfortunately only a short period of time was available and the sky conditions were not photometric. Hence the observations are used only to identify the bluest star via relative photometry. The data reduction was done using the TESTPHOT software package based on DAOPHOT (Stetson 1987). This package is in NOAO's Image Reduction and Analysis Facility (IRAF).[1]

Inserting a Fabry-Perot (F.P.) interferometer and an interference filter in the focal reducer transforms it into a F.P. camera (Joncas & Roy 1984). The scanning F.P. interferometer has a reflectivity of 93%, a FWHM of 0.024 nm (11 km s^{-1}) and a free spectral range of 0.86 nm (391.9 km s^{-1}) at Hα. We obtained three Hα interferograms of the H II region. The observations were done by setting the interferometer at three different spacings, no scanning was attempted. Each interferogram consisted of five 2000 s exposures. Reference interferograms were obtained via a hydrogen calibration lamp to calculate the nebular radial velocity. These were taken before and after each set of exposures. Comparison of the reference interferograms indicated the absence of any interferometer drifts during the exposures.

The CCD frames were preprocessed using the CCDRED package of IRAF. The interferograms were processed using a special package written by one of us (DD) within the IRAF environment. The procedure follows closely the one described in Joncas & Roy (1984). The old software was rewritten in order to benefit from IRAF's efficient program libraries and interfaces for graphics and image display. This enabled an improvement of the accuracy of the velocity measurements by a factor of two (2 km s^{-1} at a signal-to-noise level larger than 6). We will now review briefly the major steps needed to produce a velocity map.

The first step consists on calculating the position of the center of the F.P. rings for each interferogram. We use the fact that a calibration ring is circular to fit a circle through every point defining the different rings contained in the interferogram. This is done through an iteration process for better accuracy. The task is called "GETPOINTS." It uses a "SETUP" program where the user specifies the detection parameters (threshold, contrast, feature width...) for optimum detection. Then, from a given approximate center, radial vectors are constructed using standard IRAF image interpolation routines. When the vector approaches a ring, the intensity rises, reaching a maximum which corresponds to the ring's central position. The intensity decreases down to the continuum level and the vector pursues its quest for the next ring and so on until it encounters the edge of the detector. The extracted vector is then processed through a peak detection algorithm to find the exact position of the rings. Once the angular scan is finished, a circle is fitted to every ring providing a more accurate center position. The new center is fed into the program until the desired precision is obtained. The final center is calculated by averaging the centers of the first three innermost rings. The results from both calibrations are compared. If they are dissimilar (F.P. drift), the data is discarded; if not the results are averaged. The difference in the center position was always less than 0.1 pixel (0.7 to 1.3 km s^{-1}). This averaged center is used to get the peak positions in the object interferogram. Of course, in this case circles are not fitted to the rings. Next, all "defects" (stars, border effects...) are removed from the peak list. This is done interactively with the task "REMOVESTAR."

Finally, the velocity at each point is calculated from the radial difference between the ring crossing the object and the appropriate calibration ring (Joncas & Roy 1984). This task is called "VELOCITY." The end product is a table containing the velocities and their location. The velocities are corrected to the local standard of rest before repeating the whole process for each interferometer spacing. The different tables were brought to the same arbitrary reference position before further analysis outside of IRAF.

2.2. *Radio*

The aperture synthesis radio telescope of the Dominion Radio Astrophysical Observatory (DRAO), described by Roger et al. (1973) and Veidt et al. (1985), was used in this study of Sh 187. It consisted for these observations (1986 September–October) of four 9 m antennas aligned on a 600 m east-west baseline. Two continuum bands, at 408 and 1420 MHz, and the H I spectral band were observed simultaneously. The

[1] IRAF is distributed by the National Optical Astronomy Observatories, which is operated by the Association of Universities for Research in Astronomy, Inc. (AURA) under cooperative agreement with the National Science Foundation.

© American Astronomical Society • Provided by the NASA Astrophysics Data System

1992ApJ...387..591J

TABLE 1

OBSERVATIONAL PARAMETERS

Parameter	408 MHz	1420 MHz
Field of view (to 20%)	8°.06	2°.60
Synthesized beam (FWHM) (EW × NS)	3'.5 × 3'.9	1'.00 × 1'.13
Polarization	Right circular	Left circular
Calibrators and fluxes		
3C 147	48.0 Jy	23.3 Jy
3C 295	54.0 Jy	
3C 309.1		7.7 Jy
S7		100 K T_b
Continuum observed rms noise (field center)	16 mJy beam^{-1}	0.7 mJy beam^{-1}
Bandwidth	4 MHz	15 MHz
HI spectral line		
Number of chanels		128
Channel separation		0.824 km s^{-1}
Channel resolution		1.32 km s^{-1}
LSR velocity (ch. 65)		−15.0 km s^{-1}
Observed RMS noise		4.9 K
Field center (B1950)	$\alpha = 1^h21^m$ $\delta = 61°52'$	

observational parameters are listed in Table 1. The flux densities for the calibrators are from Baars et al. (1977).

The measurement of the inner portion of the *u-v* plane is not possible with a synthesis telescope. To fill the gap single antenna observations were used. For the continuum, the galactic plane surveys of Kallas & Reich (1980) at 1400 MHz and of Haslam et al. (1982) at 408 MHz were used for the central 107λ and 23λ of the *u-v* plane, respectively. For the H I line, observations were obtained with the DRAO 26 m dish. Its spectrometer has the same characteristics as the interferometer's spectral correlators. A map was made using frequency switching and calibrating with the standard region S7 (Williams 1973).

The map synthesis was done using the same procedure outlined in § 3 of Joncas & Higgs (1990).

3. OPTICAL OBSERVATIONS

3.1. *Stellar Photometry*

Our goal was to identify the exciting star of the H II region. Table 2 lists the 11 stars which appeared in all three photometric bands. The columns are self-explanatory. The statistical uncertainties are ±0.06 in *B*, ±0.03 in *V*, and ±0.04 in *R*. Four stars (no. 4, 5, 6, and 7) are within Sh 187. The star closest to the core of the H II region is also the bluest (no. 4). Its position is indicated in Figures 1 and 2. Unfortunately the lack of information on the color excess of each star prevents us from confidently selecting this star as the source of the ionizing photons. In addition, our relatively short exposure time may have prevented the detection of highly reddened stars. Figure 1 is a combination of three 180 s *I* frames. This picture was taken under good sky conditions to help in eliminating the stars present in the Hα interferograms. Faint stars which did not appear in the photometry frames are now detectable within the core of the H II region. They may be members of the Sh 187 cluster. Clearly more observations are needed.

TABLE 2

PHOTOMETRIC DATA FOR STARS IN THE Sh 187 FIELD

Number	*V*	*B*−*V*	*V*−*R*
1	15.72	1.12	0.54
2	17.58	1.22	0.75
3	13.81	0.85	0.36
4	13.64	1.24	0.60
5	15.64	1.57	0.93
6	13.69	1.46	0.98
7	14.61	1.46	0.85
8	15.62	1.12	0.46
9	15.11	1.30	0.68
10	14.64	0.97	0.43
11	15.90	1.78	1.24

3.2. *The* Hα *Morphology*

An Hα contour map of Sh 187 is shown in Figure 2 (the continuum emission was not subtracted). The contour values are in analog-digital units (1 ADU = 8.7*e*). The object is about 220″ × 120″ (EW × NS), it is composed of a bright core accompanied by faint nebulosity extending to the east and west. Unlike the bright core, this faint emission is readily seen in both red and blue POSS plates. South of the core is a group of three stars (no. 6, 7, and an unidentified one here blended with 7) to which extended emission is also adjacent. The bright core (composed of two main fragments surrounded by diffuse emission) is about 70″ × 50″ (EW × NS) in extent. These fragments are located in the eastern half where steep emission gradients suggest the presence of ionization fronts. An emission trough is running up to the middle of the core from the southern border. As will be shown later the optically visible portion of the H II region is only a fraction of the total extent of the ionized gas.

3.3. *The* Hα *Velocity field*

The F.P. interferograms yielded the measurement of 192 velocity points across the object. A histogram of the radial velocities corrected for both Earth and Sun motions (V_{lsr}) is presented in Figure 3. The mean V_{lsr} is -17.8 ± 0.9 km s^{-1}. To our knowledge we give here the first optical velocity measurements for this object. Taking into account the difference in sampling, our result is in agreement with Rossano (1978). The optically visible ionized gas is thus slightly blueshifted with respect to the molecular cloud (2.8 km s^{-1}). The standard deviation of the Hα velocities is 16.61 ± 0.8 km s^{-1}. This is

© American Astronomical Society • Provided by the NASA Astrophysics Data System

1992ApJ...387..591J

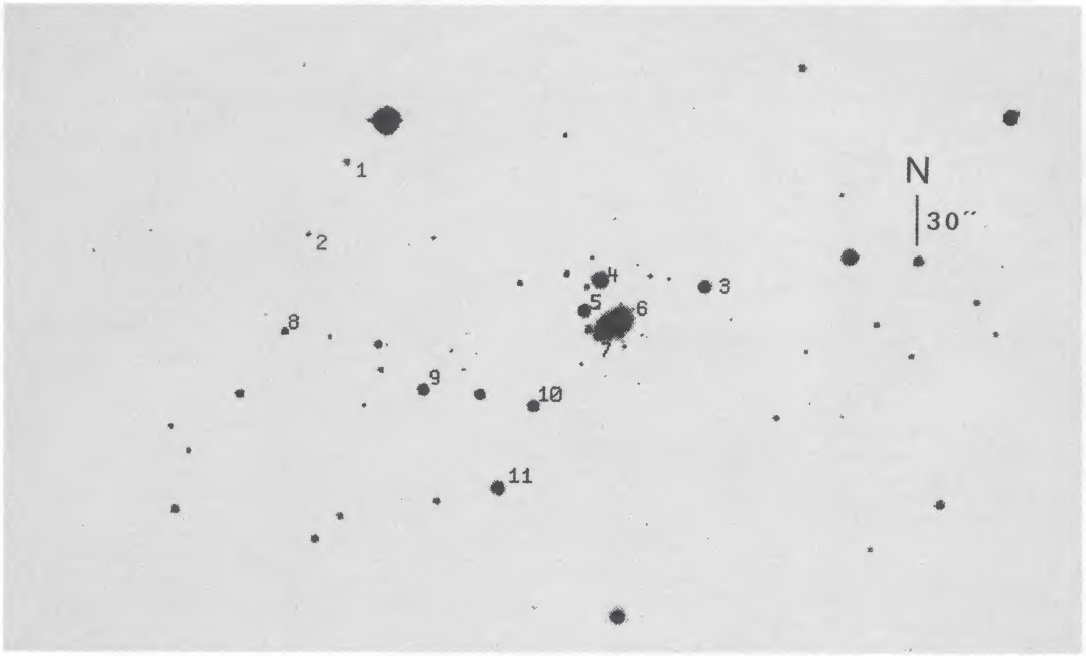

FIG. 1.—Gray scale representation of the stars in the Sh 187 field. This picture results from the combination of three 180 s exposures on a CCD through an *I* filter. The scale is 3.″6 mm^{-1} and north is up.

large considering the extent of the nebula. Looking at the histogram we note that the velocity distribution is far from being Gaussian. This shape is due to the peculiar velocity field of Sh 187.

The three interferograms cross Sh 187 from east to west (see Fig. 2). The southern one shows two-component Hα profiles. The mean component separation is 27 km s^{-1}. The central interferogram, passing almost through the middle of the object, has the same kind of profiles but this time separated by 33 km s^{-1}. For the northern interferogram most of the profiles have a single component. The profile behavior prompted us to make a plot (not shown) of the radial velocities versus the radial position (the center of the nebula was the origin). No indication of a bubblelike expansion (or contraction) of the H II region was found. Hence V_{lsr} maps were made with 10 km s^{-1} steps. Smaller velocity steps (5 km s^{-1}) reveal no further information. Figure 4 is composed of six panels covering the −50 to +10 km s^{-1} velocity range. Figures 2 and 4 have different scales and reference points. Therefore fiducial points were drawn to enable comparisons. The data points are almost exclusively from the bright core. The velocity field can be divided into three intervals: the molecular cloud interval (−20 to −10 km s^{-1}), the blueshifted interval (−40 to −20 km s^{-1}), and the

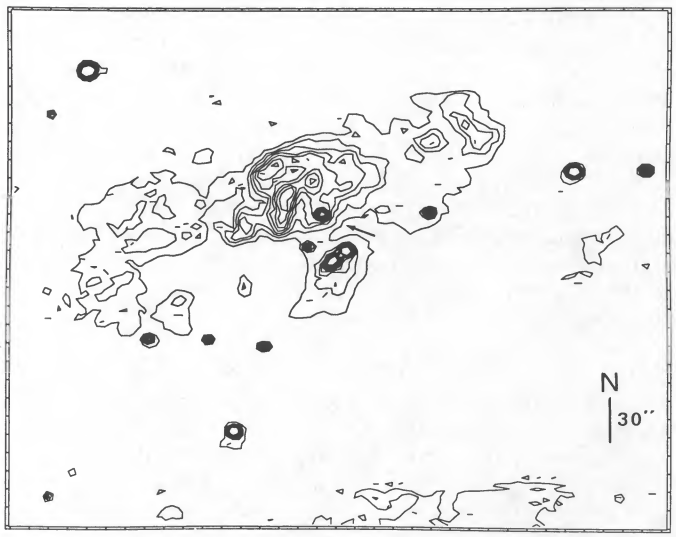

FIG. 2.—Hα contour map of Sh 187. This picture results from the combination of three 2000 s exposures on a CCD using a f/8 to f/3.5 focal reducer. The arrow points to the position of the possible exciting star. The lowest contour is at 40 ADU and the contour interval is 10 ADU. The scale is 2.″7 mm^{-1} and north is up.

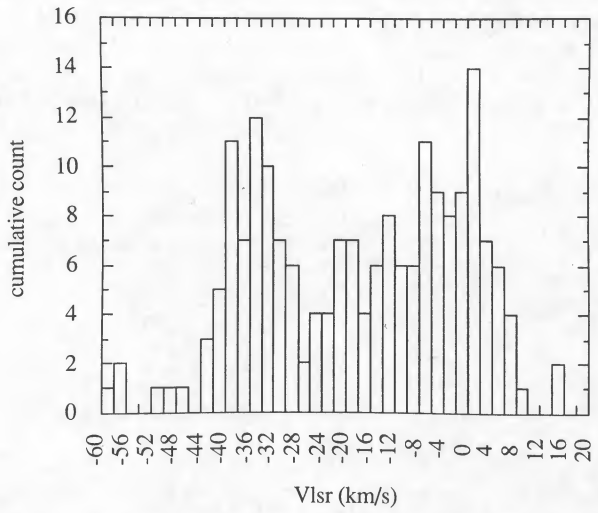

FIG. 3.—Histogram of the 192 Hα velocity points (V_{lsr}) measured across Sh 187.

© American Astronomical Society • Provided by the NASA Astrophysics Data System

1992ApJ...387..591J

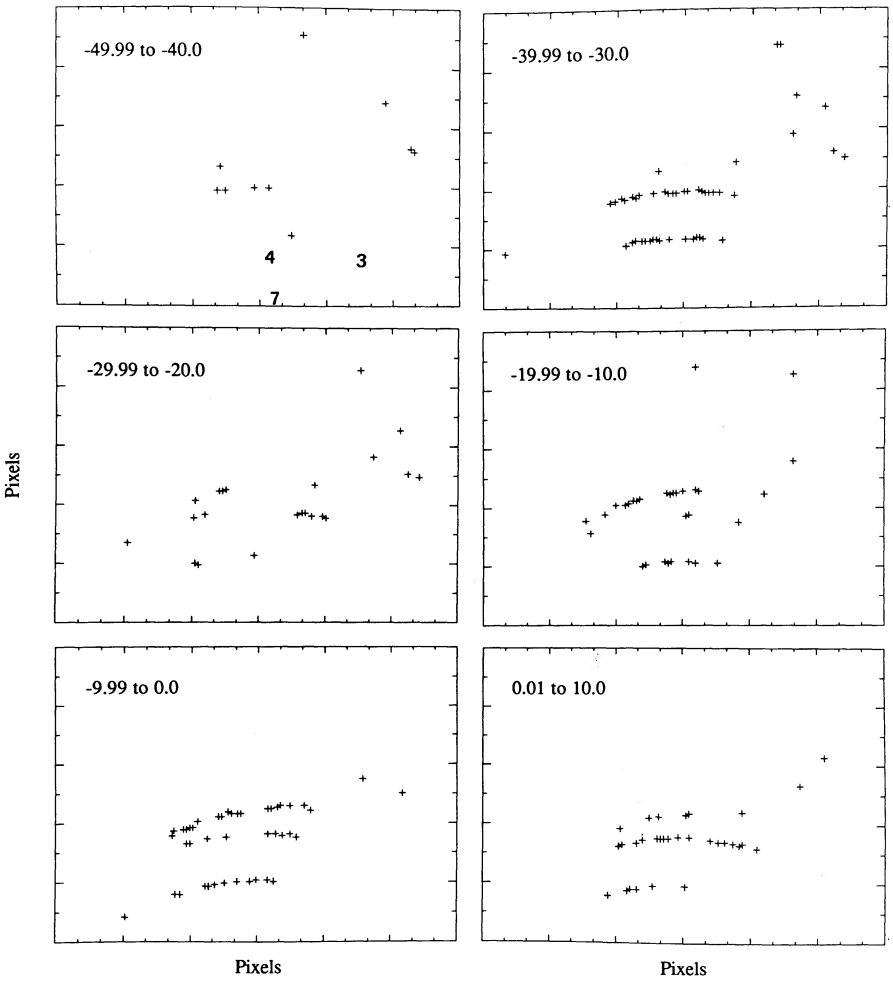

FIG. 4.—Hα V_{lsr} maps of Sh 187 in steps of 10 km s^{-1}. The numbers in the lower part of the first frame indicate the position of a few stars as fiducial marks. The velocity interval is indicated in the upper left corner.

redshifted interval (-10 to $+10$ km s^{-1}). We chose the mean velocity of the molecular cloud (-15.0 km s^{-1}) as the systemic velocity of this gas complex. There are no velocity gradients across the nebula within these velocity intervals. Moreover within given areas velocity points from each interval can be found. The blue interval has a well defined velocity range (there are few points in the -29.99 to -20.0 km s^{-1} panel) and is found mainly in the middle and southern portion of the bright core. The red interval is found everywhere and its velocity range is not as extended as the blue interval (there are no points with velocities greater than 10 km s^{-1}). The transition is smooth from -20 to $+10$ km s^{-1} in the northern and southern parts. There are very few points in the molecular cloud velocity interval from the area between the two Hα fragments. Comparisons with the overall Hα picture of the nebula show no specific correlations between the different velocity intervals and the fragments. Sh 187 could be composed of kinematically distinct H^+ flows produced by partially ionized globules and the molecular cloud.

In the faint extension west of the bright core, there is a small area bright enough to have been sampled by the F.P. interferometer. Within this area, most of the velocity points are blue-shifted with respect to the molecular cloud.

4. RADIO CONTINUUM OBSERVATIONS

4.1. Sh 187

Sh 187 was observed at both 408 and 1420 MHz. However the 408 MHz emission is strongly affected by the presence of a 2 Jy nonthermal radio source located 3.′5 south of the peak thermal emission. Therefore these observations will not be presented. Figure 5 is a superposition of the 1420 MHz continuum map on a reproduction of the relevant E plate of the POSS. The first contour is at the 2 mJy beam^{-1} level (3 σ). Its dented appearance at the southern edge is an artefact originating from the subtraction of the nonthermal point source mentioned above. The small peak at the northern edge is another point source ($Sv = 9 \pm 4$ mJy). Since the source could not be resolved with the 408 MHz observations, a spectral index cannot be derived. The exact nature of this source remains undetermined. The H II region is almost circular with a diameter of 7′ (3 σ level). It has a peak brightness temperature of 17 ± 2 K (1 σ error) located at $\alpha = 1^h19^m50^s$, $\delta = 61°37'11''$ (1950 coordinates).

There is little correspondence between the radio map and the optical emission (Fig. 5). Part of the ionized gas is invisible due to the presence of intervening absorbing material.

© American Astronomical Society • Provided by the NASA Astrophysics Data System

1992ApJ...387..591J

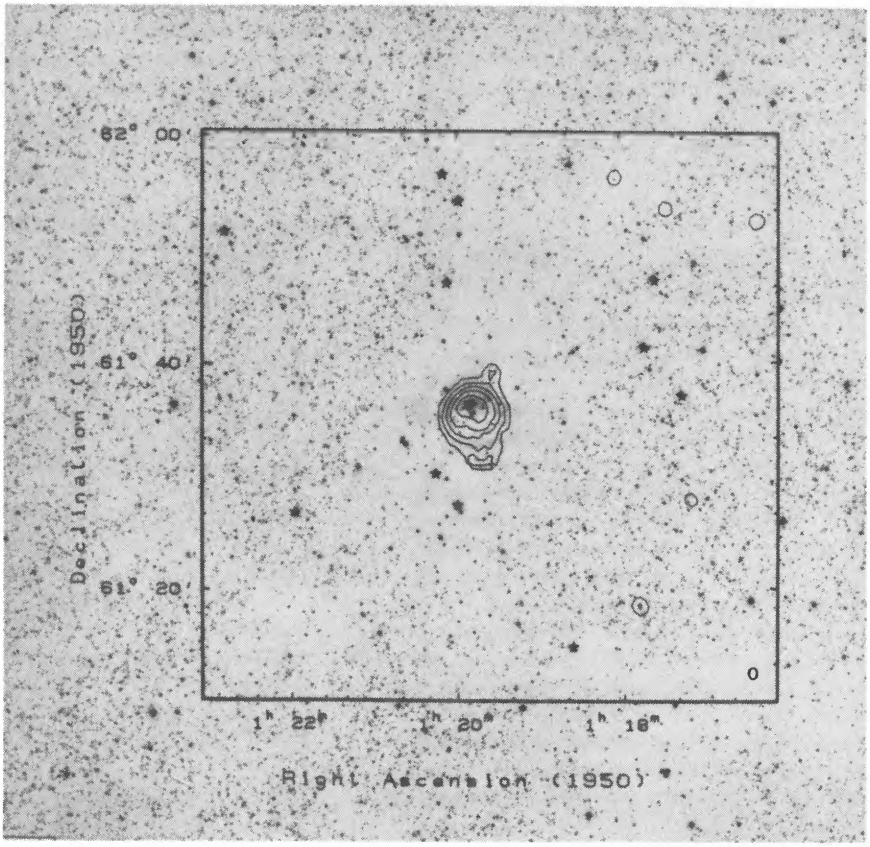

FIG. 5.—Radio continuum map of Sh 187 at 1.4 GHz. The half-power beamwidth is shown in the lower right hand corner. The contours are 2.0, 15.0, 30.0, 50.0, 90.0 mJy beam^{-1}. The dented contour results from the subtraction of a strong extragalactic compact source. The peak brightness temperature is 17 K.

However the peak radio continuum emission coincides with the bright core of the optical nebula. The total radio flux density of Sh 187 at 1420 MHz is 1.15 ± 0.12 Jy. This is in good agreement with the single dish measurements of Felli & Churchwell (1972) after subtraction of the two point sources' contribution (0.5 Jy). Combining the flux density with the electron temperature from Rossano (1978) we obtain an excitation parameter (Schraml & Mezger 1969) of 13 ± 2 cm^{-2} pc. The uncertainty comes essentially from the inaccurate knowledge of the kinematical distance to the object (10%–25%, see discussion in Fich & Blitz 1984). Comparing the value of the excitation parameter with the results from the modeling of Panagia (1973), we obtain a spectral type of B0.5 for the exciting star. One must keep in mind that since the nebula is not completely ionization bounded the true spectral type may be somewhat earlier. Moreover new evidence (Voels et al. 1989) suggest that Panagia's computations require some corrections while there is also the distinct possibility that ionization may be produced by a cluster, not a single B0.5 star.

In order to derive the mass and density for the nebula, a model must be proposed for the distribution of matter. The nebula was divided into eight sectors centered on the radio continuum peak to get a better idea of the emission distribution. The mean value of every pixel, having the same radius, was calculated inside each sector. Putting aside the two sectors corrupted by the point sources, we established the distribution to be Gaussian. The mean half-width at half-maximum (HWHM) is 1.'6 (1 σ = 0.'4). We thus have $n(r) = n(0) \exp [-r^2/(0.6g)^2]$ for the distribution, where r is the radius in arcminutes, g is the FWHM and $n(0)$ is the maximum density. Following Mezger & Henderson (1967) we derive $n(0) = 100$ cm^{-3} and a total mass of ionized material (H + He) of 7 $M_\odot$. Putting aside for now the uncertainty due to the modeling, the main source of error for these numbers comes again from the distance uncertainty. The mass determination is the most affected with a corresponding uncertainty of $\pm 45\%$, while the density has an uncertainty of $\pm 10\%$. Looking now at the model, the observed Gaussian density distribution may be caused by the finite synthesized beam size. Assuming Sh 187 to be instead a spherical H II region with a uniform density, its mass would be two times smaller. Even with a change in models, the mass estimates stay within the uncertainty. We can obviously call these models an oversimplification of reality. The Hα picture of Figure 2 reveals the core of the nebula to be relatively clumpy. If this is the case over the whole object [clumpy H II regions are not uncommon (see Felli, Churchwell, & Massi 1984 and Kassim et al. 1989)], then $n(0)$ and the mass are respectively underestimated and overestimated. In fact the appearance of the nebula in the high-resolution VLA map of Snell & Bally (1986) seems to confirm this hypothesis. The VLA map also helps us rejecting more sophisticated multicomponent models such as, for example, a core-halo morphology. The presence of clumps on any scale will make things average out in a Gaussian-like fashion.

4.2. *Other Continuum Sources*

Lists of small-diameter sources found in the two continuum fields are given in Tables 3 (408 MHz) and 4 (1420 MHz). For

© American Astronomical Society • Provided by the NASA Astrophysics Data System

1992ApJ...387..591J

TABLE 3

408 MHz COMPACT SOURCES

Source	Right Ascension (1950)	+/-	Declination (1950)	+/-	Flux Density (mJy)	+/-	Size	P.A.	Other Designation
3OP01	OH 49M 06.0S	1.7S	62D 37' 10"	14"	367	36			GT0049+626
3OP02	OH 50M 35.0S	2.4S	62D 45' 01"	18"	268	49	4.8' x 2.5'	-39d	
3OP03*	OH 52M 45.0S	2.4S	59D 02' 21"	39"	696	239			
3OP04	OH 53M 38.4S	1.4S	62D 25' 56"	12"	520	22			GT0053+624
3OP05	OH 54M 36.6S	1.4S	59D 56' 34"	12"	1027	35			BG0054+60
3OP06	OH 54M 42.4S	1.4S	62D 55' 45"	12"	643	33			GT0054+629
3OP07	OH 54M 43.8S	1.5S	60D 47' 41"	13"	405	29			
3OP08	OH 55M 00.0S	1.7S	61D 57' 46"	16"	102	21			
3OP09	OH 56M 15.4S	1.5S	63D 56' 38"	12"	668	37			GT0056+639, 4C63.03
3OP10*	OH 56M 26.0S	1.7S	58D 41' 30"	16"	263	87			
3OP11	OH 56M 26.5S	1.5S	61D 59' 46"	13"	267	21			
3OP12	OH 56M 48.0S	1.7S	59D 37' 43"	20"	357	60			
3OP13	OH 57M 26.3S	1.4S	64D 14' 16"	12"	1017	44			KR112, GT0057+642
3OP14	OH 57M 28.0S	2.4S	64D 54' 44"	17"	173	51			
3OP15	OH 58M 20.1S	1.6S	59D 28' 38"	15"	206	58			
3OP16	OH 58M 31.3S	1.5S	63D 42' 02"	12"	842	49			GT0058+637
3OP17*	OH 59M 19.1S	1.4S	65D 24' 05"	12"	1074	44			KR113
3OP18*	OH 59M 43.9S	1.5S	58D 08' 06"	12"	753	58			BG0059+58
3OP19	OH 59M 52.1S	1.7S	62D 47' 37"	13"	299	83			
3OP20	1H 00M 06.7S	1.5S	63D 06' 57"	14"	447	36	4.9' x 2.2'	86d	GT0100+631
3OP21	1H 00M 12.0S	1.7S	63D 52' 51"	16"	164	27			
3OP22	1H 00M 38.0S	1.7S	62D 51' 59"	14"	188	56			GT0100+628
3OP23	1H 01M 27.0S	4.2S	60D 52' 16"	27"	109	49			
3OP24	1H 01M 44.5S	1.7S	60D 23' 07"	13"	293	31			
3OP25	1H 01M 58.0S	1.6S	62D 59' 26"	13"	195	22			
3OP26	1H 02M 01.0S	3.3S	58D 55' 08"	21"	160	47			
3OP27	1H 02M 29.8S	1.7S	59D 07' 29"	16"	1116	47			
3OP28	1H 02M 55.5S	1.5S	59D 59' 19"	13"	209	17			
3OP29*	1H 03M 03.0S	1.7S	65D 37' 46"	15"	385	112			
3OP30	1H 03M 19.2S	1.4S	63D 10' 04"	12"	1452	53			GT0103+631, BG0103+63
3OP31	1H 03M 43.9S	1.5S	61D 26' 54"	13"	341	25			GT0103+614
3OP32*	1H 04M 13.0S	2.4S	58D 20' 25"	29"	255	77	5.8' x 2.5'	123d	
3OP33	1H 04M 18.9S	1.5S	58D 56' 12"	13"	253	28			
3OP34	1H 04M 45.0S	1.7S	63D 30' 32"	17"	109	33			
3OP35	1H 04M 53.0S	6.2S	58D 46' 37"	20"	99	53			
3OP36*	1H 05M 18.9S	1.5S	58D 11' 43"	13"	612	45			
3OP37	1H 05M 25.0S	1.7S	63D 47' 06"	14"	143	27			
3OP38	1H 05M 34.6S	1.4S	61D 04' 38"	12"	1017	43			KR116, BG/GT0105+610, 4C61.01
3OP39	1H 05M 38.5S	1.4S	64D 35' 40"	12"	583	29			
3OP40	1H 06M 36.4S	1.5S	61D 17' 29"	12"	277	20			GT0106+613
3OP41	1H 06M 52.9S	1.5S	59D 41' 45"	12"	333	91			
3OP42	1H 07M 40.4S	1.4S	60D 16' 29"	12"	1919	82			KR117, 4C60.04
3OP43	1H 07M 42.0S	4.2S	59D 21' 57"	22"	198	73	6.6' x 2.6'	-10d	
3OP44*	1H 07M 52.5S	1.6S	56D 16' 07"	13"	3058	349			
3OP45	1H 08M 02.0S	3.3S	65D 16' 54"	18"	360	82	5.8' x 3.2'	27d	
3OP46	1H 08M 07.5S	1.4S	59D 07' 10"	12"	1630	58			4C59.01
3OP47	1H 08M 10.6S	1.6S	62D 36' 30"	14"	110	14			
3OP48	1H 08M 30.0S	2.4S	59D 36' 42"	18"	53	15			
3OP49	1H 08M 33.9S	1.4S	62D 25' 23"	12"	378	102			
3OP50	1H 08M 38.0S	1.4S	58D 06' 41"	12"	925	49			4C58.03
3OP51	1H 09M 22.2S	1.4S	61D 20' 23"	12"	604	26			KR118, GT0109+613
3OP52 (02)	1H 10M 38.9S	1.4S	62D 08' 31"	12"	1259	44			KR119, 4C62.02, GT0110+621
3OP53	1H 11M 15.3S	1.6S	59D 03' 54"	13"	299	27	3.5' x 1.9'	-20d	
3OP54	1H 11M 35.8S	1.5S	60D 32' 22"	13"	209	20			
3OP55 (09)	1H 12M 42.0S	1.7S	62D 49' 18"	14"	74	13			
3OP56	1H 12M 48.0S	2.4S	58D 55' 28"	23"	94	33			
3OP57	1H 13M 11.0S	2.4S	59D 41' 05"	14"	201	36			
3OP58	1H 13M 27.0S	2.4S	58D 16' 13"	17"	232	49			
3OP59	1H 13M 27.1S	1.6S	58D 39' 33"	18"	208	35			
3OP60	1H 13M 39.3S	1.6S	60D 26' 22"	16"	126	24			
3OP61	1H 13M 54.8S	1.6S	59D 10' 38"	13"	355	41			
3OP62	1H 14M 39.0S	1.7S	59D 36' 02"	13"	152	27			
3OP63	1H 14M 44.0S	2.4S	59D 21' 23"	23"	96	45			
3OP64	1H 15M 00.9S	1.4S	63D 14' 33"	12"	709	26			GT0114+632
3OP65	1H 16M 23.0S	1.7S	58D 22' 33"	18"	195	61			
3OP66	1H 16M 25.8S	1.5S	60D 23' 26"	13"	282	20			
3OP67	1H 16M 41.7S	1.5S	59D 27' 50"	13"	244	18			
3OP68	1H 17M 35.3S	1.6S	58D 26' 42"	14"	189	56			
3OP69	1H 17M 42.4S	1.7S	64D 57' 44"	16"	277	78			
3OP70 (35)	1H 18M 10.5S	1.5S	62D 01' 49"	13"	193	27			GT0118+620
3OP71	1H 18M 30.6S	1.5S	65D 09' 16"	12"	305	22			
3OP72 (38)	1H 18M 40.6S	1.5S	60D 44' 28"	13"	248	25			GT0118+607
3OP73	1H 19M 18.1S	1.6S	63D 51' 43"	13"	556	61			GT0119+638
3OP74	1H 19M 23.0S	2.4S	60D 08' 54"	16"	168	47			
3OP75 (42)	1H 19M 43.4S	1.4S	61D 33' 29"	12"	2320	135			KR120, 4C61.02, BG0119+61
3OP76	1H 20M 20.9S	1.4S	59D 15' 19"	12"	464	23			
3OP77	1H 20M 37.9S	1.5S	63D 26' 18"	13"	153	14			
3OP78 (46)	1H 20M 39.0S	1.4S	61D 00' 14"	12"	651	25			
3OP79	1H 21M 56.1S	1.6S	57D 52' 06"	15"	541	155			
3OP80	1H 22M 07.4S	1.5S	57D 58' 22"	14"	636	182			

© American Astronomical Society • Provided by the NASA Astrophysics Data System

1992ApJ...387..591J

TABLE 3—*Continued*

Source	Right Ascension (1950)	+/-	Declination (1950)	+/-	Flux Density (mJy)	+/-	Size	P.A.	Other Designation
30P81	1H 22M 09.3S	12.1S	59D 02' 12"	52"	306	89			
30P82	1H 22M 12.2S	1.4S	64D 23' 41"	12"	441	23			
30P83	1H 22M 42.6S	1.4S	63D 57' 52"	12"	278	13			GT0122+639
30P84	1H 23M 26.0S	1.7S	63D 33' 55"	15"	117	17			
30P85 (55)	1H 23M 30.4S	1.4S	61D 36' 35"	12"	430	21			
30P86	1H 23M 42.4S	1.4S	59D 56' 01"	12"	606	22			
30P87 (57)	1H 24M 16.5S	1.4S	61D 19' 02"	12"	822	31			GT0124+613
30P88	1H 24M 34.0S	1.7S	65D 09' 42"	13"	259	31			
30P89	1H 24M 44.6S	1.5S	59D 23' 57"	13"	220	22			
30P90	1H 25M 19.0S	1.7S	65D 04' 54"	16"	189	56			
30P91	1H 25M 27.5S	1.4S	60D 00' 50"	12"	422	19			
30P92	1H 25M 36.3S	1.4S	60D 33' 18"	12"	255	17			GT0125+605
30P93	1H 25M 39.0S	1.7S	64D 12' 14"	18"	292	44			
30P94	1H 25M 59.8S	1.4S	63D 59' 21"	12"	418	21			
30P95	1H 26M 09.0S	2.4S	63D 38' 54"	16"	132	43			
30P96	1H 26M 20.4S	1.4S	64D 31' 04"	12"	623	28			
30P97 (72)	1H 26M 50.7S	1.6S	61D 38' 12"	13"	153	19			
30P98	1H 27M 11.6S	1.4S	58D 18' 54"	12"	1621	57			BG0127+58, 4C58.05
30P99	1H 27M 18.1S	1.5S	63D 46' 52"	12"	348	95			GT0127+637
30P100(76)	1H 28M 00.0S	1.5S	62D 42' 35"	12"	362	24			
30P101	1H 28M 27.8S	1.5S	60D 23' 45"	13"	385	40			GT0128+604
30P102	1H 29M 04.4S	1.4S	65D 44' 42"	12"	1616	83			KR121, BG0129+65, 4C65.01
30P103(79)	1H 29M 13.4S	1.5S	62D 27' 53"	12"	281	17			GT0129+624
30P104	1H 30M 24.4S	1.7S	65D 17' 01"	14"	222	27			
30P105	1H 30M 27.7S	1.5S	59D 07' 31"	13"	212	24			
30P106	1H 30M 31.0S	1.7S	63D 18' 23"	14"	58	20			
30P107	1H 30M 49.7S	1.5S	63D 42' 46"	12"	238	16			GT0130+636
30P108	1H 31M 37.6S	1.4S	65D 09' 32"	12"	804	37			
30P109	1H 31M 51.0S	1.5S	59D 19' 16"	13"	297	82			
30P110	1H 31M 57.4S	1.7S	60D 03' 22"	14"	119	16			
30P111*	1H 32M 37.4S	1.7S	58D 03' 36"	14"	298	67			
30P112	1H 32M 57.9S	1.4S	61D 01' 14"	12"	662	26			GT0132+610
30P113	1H 33M 24.8S	1.4S	62D 47' 16"	12"	508	147			GT0133+637
30P114	1H 33M 35.2S	1.6S	60D 16' 52"	13"	993	36			GT0133+602
30P115	1H 33M 41.3S	1.6S	64D 40' 33"	13"	389	31	3.1' x 2.3'	109d	
30P116	1H 33M 51.4S	2.2S	59D 22' 19"	16"	77	24			
30P117	1H 33M 51.8S	1.5S	61D 13' 35"	13"	267	19			
30P118	1H 34M 17.9S	1.6S	64D 11' 52"	14"	114	20			
30P119*	1H 34M 31.5S	1.7S	57D 59' 05"	14"	274	59			
30P120	1H 34M 38.8S	1.5S	62D 44' 06"	12"	340	35			GT0134+627
30P121	1H 34M 42.4S	1.5S	65D 06' 39"	12"	1080	74			4C65.07
30P122	1H 34M 43.3S	1.7S	62D 01' 24"	16"	153	43			
30P123	1H 34M 45.2S	2.1S	58D 24' 09"	23"	205	72			
30P124	1H 34M 55.0S	1.7S	63D 25' 25"	15"	115	19			
30P125	1H 35M 05.0S	1.7S	63D 16' 39"	14"	150	20			
30P126	1H 35M 51.1S	1.4S	60D 40' 53"	12"	775	29			KR126, GT0135+606
30P127	1H 36M 23.7S	3.0S	59D 16' 13"	18"	268	67			
30P128	1H 37M 01.5S	1.7S	62D 52' 05"	14"	99	15			
30P129	1H 37M 26.2S	1.4S	64D 25' 57"	12"	491	27			KR124
30P130	1H 37M 33.3S	1.6S	61D 51' 34"	13"	145	18			GT0137+618
30P131	1H 37M 49.2S	1.4S	60D 14' 21"	12"	561	24			GT0137+602
30P132	1H 38M 17.0S	1.5S	65D 26' 21"	13"	657	55			
30P133	1H 38M 29.9S	2.4S	59D 55' 45"	16"	1102	42			
30P134*	1H 38M 30.3S	2.4S	57D 53' 08"	18"	310	109			
30P135*	1H 38M 43.2S	1.4S	58D 03' 40"	12"	3083	120			BG0138+58, 4C58.06
30P136	1H 39M 05.0S	1.7S	64D 14' 54"	18"	203	40			
30P137	1H 39M 11.6S	1.4S	61D 10' 25"	12"	378	20			GT0139+611
30P138*	1H 39M 58.5S	1.6S	58D 21' 32"	13"	389	46			
30P139	1H 40M 00.0S	1.6S	61D 55' 29"	13"	118	15			
30P140	1H 40M 00.1S	1.6S	65D 46' 54"	13"	364	103			
30P141	1H 40M 18.4S	1.5S	60D 19' 22"	12"	345	21			GT0140+603
30P142	1H 40M 19.3S	1.5S	61D 08' 11"	13"	238	16			
30P143	1H 40M 54.5S	1.5S	61D 21' 49"	13"	147	14			
30P144	1H 41M 11.0S	1.7S	62D 22' 13"	16"	119	21			
30P145	1H 42M 13.7S	1.6S	62D 37' 15"	13"	210	23			
30P146	1H 43M 20.6S	1.5S	63D 49' 52"	12"	280	17			
30P147	1H 43M 27.4S	1.5S	64D 05' 02"	12"	311	21			
30P148	1H 44M 15.6S	1.5S	60D 10' 56"	12"	466	33			GT0144+601
30P149*	1H 44M 21.2S	1.7S	58D 25' 44"	15"	754	99			
30P150	1H 44M 28.3S	1.5S	64D 56' 41"	13"	713	51	4.1' x 1.4'	107d	
30P151	1H 44M 41.6S	1.5S	63D 29' 40"	12"	292	21			
30P152	1H 45M 49.1S	1.5S	60D 22' 04"	13"	233	20			
30P153	1H 45M 57.0S	1.7S	64D 49' 06"	14"	349	52			
30P154	1H 46M 04.7S	1.5S	61D 35' 13"	13"	220	19			
30P155	1H 47M 29.1S	1.5S	63D 43' 39"	13"	543	39			GT0147+637
30P156*	1H 47M 49.0S	1.7S	65D 08' 50"	17"	407	78			
30P157	1H 48M 18.3S	1.4S	61D 02' 13"	12"	500	24			GT0148+610
30P158*	1H 48M 26.6S	1.4S	64D 39' 30"	12"	1567	61			KR127AB, BG0148+64, 4C64.01
30P159	1H 49M 35.1S	1.5S	63D 57' 15"	13"	443	32			
30P160	1H 49M 35.5S	1.6S	62D 29' 50"	13"	528	49			GT0149+625
30P161*	1H 49M 48.1S	1.6S	59D 35' 21"	14"	335	45			
30P162	1H 51M 24.4S	1.5S	62D 04' 14"	13"	1651	449			KR129, GT0151+620, 4C62.03
30P163*	1H 55M 07.8S	1.4S	60D 46' 23"	12"	1061	57			KR132, GT0155+607

NOTES.—(nn) Indicates source is number 31Pnn in 1420 MHz list (Table 4). Asterisk (*) indicates source is outside prescribed radius. Other designations: (BG) Fanti et al. 1974; (GT) Gregory & Taylor 1986; (KR) Fich 1986; (4C) Gower et al. 1967.

© American Astronomical Society • Provided by the NASA Astrophysics Data System

1992ApJ...387..591J

TABLE 4

1420 MHz COMPACT SOURCES

Source	Right Ascension (1950)	Declination (1950)	Flux Density (mJy)	Size	P.A.	Other Designations[a]
31P01.....	$1^h10^m29^s.5 \pm 0^s.4$	$61°49'55'' \pm 3''$	83 ± 6			
31P02.....	$1\ 10\ 35.0 \pm 0.4$	$62\ 7\ 44 \pm 3$	224 ± 8			30P52, KR 119
31P03.....	$1\ 10\ 39.0 \pm 0.4$	$62\ 0\ 50 \pm 4$	26 ± 8			
31P04.....	$1\ 10\ 43.8 \pm 0.4$	$62\ 9\ 44 \pm 3$	232 ± 15			
31P05.....	$1\ 11\ 41.9 \pm 0.7$	$62\ 13\ 42 \pm 4$	24 ± 5			
31P06.....	$1\ 11\ 53.9 \pm 0.4$	$61\ 35\ 29 \pm 3$	89 ± 4			
31P07.....	$1\ 12\ 28.9 \pm 0.6$	$61\ 50\ 46 \pm 10$	33 ± 7			
31P08.....	$1\ 12\ 34.7 \pm 0.5$	$60\ 57\ 4 \pm 2$	82 ± 10			
31P09.....	$1\ 12\ 45.6 \pm 0.6$	$62\ 49\ 22 \pm 6$	45 ± 9			30P55
31P10.....	$1\ 13\ 41.8 \pm 0.5$	$62\ 21\ 39 \pm 4$	20 ± 3			
31P11.....	$1\ 13\ 52.0 \pm 0.6$	$62\ 32\ 26 \pm 4$	19 ± 4			
31P12.....	$1\ 14\ 32.0 \pm 0.7$	$60\ 48\ 34 \pm 6$	17 ± 7			
31P13.....	$1\ 14\ 34.6 \pm 0.5$	$62\ 37\ 37 \pm 4$	34 ± 3			
31P14.....	$1\ 14\ 42.6 \pm 0.6$	$61\ 55\ 0 \pm 9$	8 ± 3			
31P15.....	$1\ 14\ 46.6 \pm 0.4$	$61\ 0\ 19 \pm 3$	81 ± 4	$0'.8 \times 0'.8$	9°	
31P16.....	$1\ 14\ 55.2 \pm 0.5$	$61\ 58\ 1 \pm 4$	11 ± 2			
31P17.....	$1\ 14\ 55.6 \pm 0.6$	$62\ 55\ 21 \pm 4$	49 ± 13			
31P18.....	$1\ 15\ 5.7 \pm 0.4$	$62\ 19\ 6 \pm 3$	188 ± 3			
31P19.....	$1\ 15\ 10.9 \pm 0.4$	$62\ 49\ 52 \pm 4$	52 ± 4	0.9×0.5	62	
31P20.....	$1\ 15\ 11.5 \pm 0.4$	$62\ 3\ 12 \pm 3$	33 ± 2			
31P21.....	$1\ 15\ 27.3 \pm 0.4$	$62\ 25\ 56 \pm 3$	97 ± 2			
31P22.....	$1\ 15\ 32.5 \pm 2.0$	$61\ 35\ 2 \pm 5$	22 ± 6			
31P23.....	$1\ 15\ 37.3 \pm 0.6$	$61\ 35\ 0 \pm 5$	10 ± 4			
31P24.....	$1\ 16\ 1.4 \pm 0.4$	$62\ 13\ 29 \pm 3$	44 ± 1			
31P25.....	$1\ 16\ 2.5 \pm 1.1$	$62\ 51\ 10 \pm 5$	46 ± 9			
31P26.....	$1\ 16\ 2.8 \pm 0.4$	$62\ 3\ 47 \pm 3$	29 ± 2			
31P27.....	$1\ 16\ 18.4 \pm 0.4$	$61\ 52\ 19 \pm 4$	14 ± 4			
31P28.....	$1\ 16\ 34.7 \pm 0.5$	$62\ 4\ 56 \pm 5$	12 ± 2			
31P29.....	$1\ 16\ 55.6 \pm 0.4$	$61\ 3\ 21 \pm 3$	62 ± 2	0.7×0.4	127	
31P30.....	$1\ 17\ 1.3 \pm 0.4$	$62\ 10\ 25 \pm 3$	69 ± 1			
31P31.....	$1\ 17\ 6.7 \pm 0.4$	$62\ 17\ 26 \pm 3$	34 ± 2			
31P32.....	$1\ 17\ 9.8 \pm 0.4$	$61\ 27\ 54 \pm 4$	15 ± 2			
31P33.....	$1\ 17\ 25.8 \pm 0.4$	$61\ 53\ 31 \pm 3$	13 ± 1			
31P34.....	$1\ 17\ 40.0 \pm 0.6$	$62\ 21\ 29 \pm 5$	8 ± 2			
31P35.....	$1\ 18\ 9.0 \pm 0.4$	$62\ 2\ 1 \pm 3$	70 ± 1			30P70
31P36.....	$1\ 18\ 18.2 \pm 0.6$	$62\ 46\ 48 \pm 6$	18 ± 4			
31P37.....	$1\ 18\ 18.2 \pm 0.6$	$62\ 15\ 33 \pm 4$	7 ± 3			
31P38.....	$1\ 18\ 40.2 \pm 0.4$	$60\ 44\ 26 \pm 3$	118 ± 4	1.3×0.6	91	30P72
31P39.....	$1\ 18\ 49.5 \pm 0.6$	$62\ 18\ 53 \pm 8$	6 ± 2			
31P40.....	$1\ 18\ 56.5 \pm 0.4$	$60\ 55\ 43 \pm 3$	138 ± 2	0.7×0.3	108	
31P41.....	$1\ 19\ 2.1 \pm 0.6$	$61\ 6\ 57 \pm 4$	9 ± 3			
31P42.....	$1\ 19\ 41.8 \pm 0.4$	$61\ 32\ 36 \pm 3$	495 ± 8			30P75, 4C 61.02, BG 0119+61
31P43.....	$1\ 19\ 50.8 \pm 0.4$	$60\ 38\ 7 \pm 4$	49 ± 4			
31P44.....	$1\ 20\ 8.5 \pm 0.4$	$62\ 10\ 23 \pm 3$	24 ± 1			
31P45.....	$1\ 20\ 37.9 \pm 0.5$	$62\ 21\ 51 \pm 4$	9 ± 2			
31P46.....	$1\ 20\ 38.4 \pm 0.4$	$61\ 0\ 14 \pm 3$	208 ± 3			30P78
31P47.....	$1\ 20\ 40.6 \pm 0.4$	$62\ 20\ 8 \pm 4$	9 ± 2			
31P48.....	$1\ 22\ 11.1 \pm 0.6$	$62\ 1\ 22 \pm 7$	6 ± 2			
31P49.....	$1\ 22\ 41.6 \pm 0.4$	$62\ 24\ 16 \pm 3$	49 ± 2			
31P50.....	$1\ 22\ 52.1 \pm 0.5$	$62\ 51\ 52 \pm 4$	31 ± 4	1.4×1.0	86	
31P51.....	$1\ 23\ 6.7 \pm 0.4$	$62\ 5\ 34 \pm 3$	70 ± 1	0.3×0.2	108	
31P52.....	$1\ 23\ 17.0 \pm 0.4$	$62\ 32\ 44 \pm 4$	14 ± 4			
31P53.....	$1\ 23\ 22.7 \pm 0.8$	$61\ 39\ 60 \pm 34$	10 ± 6			
31P54.....	$1\ 23\ 27.5 \pm 0.5$	$61\ 54\ 38 \pm 4$	7 ± 2			
31P55.....	$1\ 23\ 30.0 \pm 0.4$	$61\ 36\ 31 \pm 3$	126 ± 2			30P85
31P56.....	$1\ 23\ 42.4 \pm 0.9$	$62\ 42\ 26 \pm 6$	39 ± 5	2.8×1.3	39	
31P57.....	$1\ 24\ 15.9 \pm 0.4$	$61\ 19\ 2 \pm 3$	270 ± 2	0.5×0.2	65	30P87
31P58.....	$1\ 24\ 20.5 \pm 0.6$	$61\ 2\ 21 \pm 5$	15 ± 3			
31P59.....	$1\ 24\ 26.2 \pm 0.5$	$61\ 52\ 48 \pm 4$	12 ± 2			
31P60.....	$1\ 24\ 26.8 \pm 0.4$	$61\ 47\ 34 \pm 4$	14 ± 2			

© American Astronomical Society • Provided by the NASA Astrophysics Data System

1992ApJ...387..591J

TABLE 4—*Continued*

Source	Right Ascension (1950)	Declination (1950)	Flux Density (mJy)	Size	P.A.	Other Designations[a]
31P61.....	1 24 34.9 ± 0.6	61 53 43 ± 4	7 ± 2			
31P62.....	1 24 55.4 ± 0.4	61 44 37 ± 3	17 ± 5			
31P63.....	1 24 56.7 ± 0.4	62 46 43 ± 3	75 ± 3			
31P64.....	1 25 5.3 ± 0.5	62 24 20 ± 4	11 ± 2			
31P65.....	1 25 8.2 ± 0.4	62 50 58 ± 3	396 ± 5	0.8 × 0.2	108	
31P66.....	1 25 10.7 ± 0.5	61 34 26 ± 4	8 ± 3			
31P67.....	1 25 17.9 ± 0.4	62 16 54 ± 3	24 ± 2	0.7 × 0.5	123	
31P68.....	1 26 14.5 ± 0.4	61 57 16 ± 3	22 ± 2			
31P69.....	1 26 17.4 ± 0.4	61 0 51 ± 4	44 ± 4			
31P70.....	1 26 30.6 ± 2.0	61 34 47 ± 41	14 ± 8			
31P71.....	1 26 31.8 ± 0.4	61 8 12 ± 4	27 ± 3	0.9 × 0.6	71	
31P72.....	1 26 49.7 ± 0.4	61 38 18 ± 3	43 ± 2	1.0 × 0.3	7	30P97
31P73.....	1 26 51.8 ± 0.5	60 51 11 ± 4	34 ± 5			
31P74.....	1 27 47.0 ± 0.6	61 5 10 ± 5	21 ± 6			
31P75.....	1 27 51.0 ± 0.6	61 43 23 ± 4	11 ± 2			
31P76.....	1 27 58.5 ± 0.4	62 42 31 ± 3	96 ± 5	1.0 × 0.7	117	30P100
31P77.....	1 28 20.2 ± 0.7	62 19 50 ± 5	26 ± 4			
31P78.....	1 29 8.9 ± 0.4	61 35 34 ± 3	21 ± 2			
31P79.....	1 29 12.5 ± 0.4	62 27 44 ± 3	83 ± 4	1.0 × 0.4	122	30P103
31P80.....	1 29 15.1 ± 0.4	61 18 26 ± 3	84 ± 4			
31P81.....	1 29 36.4 ± 0.5	62 20 4 ± 4	23 ± 3			
31P82.....	1 29 42.8 ± 0.5	61 47 19 ± 4	27 ± 3	1.2 × 0.6	−5	
31P83.....	1 30 2.9 ± 0.6	61 26 53 ± 4	27 ± 5			
31P84.....	1 30 26.0 ± 0.4	62 45 44 ± 3	98 ± 6			
31P85.....	1 31 1.8 ± 0.6	60 48 56 ± 7	54 ± 17			

[a] Other designations: (30P) this work; (BG) Fanti et al. 1974; (KR) Fich 1986; (4C) Gower et al. 1967.

reference purposes the sources were given 30Pn and 31Pn numbers following the procedure described by Higgs (1986). The catalogued sources are all above the 20% level of the primary beam except for the few strong sources marked with an asterisk (*) in Table 3. Sources down to a 10 σ level of 50 mJy at 408 MHz and 7 mJy at 1420 MHz at the map center were selected for analysis with two-dimensional gaussian fits to the sources. Systematic errors were added quadratically to the fitting errors for the position (1/20 of the beamwidth) and flux (3%). The last column contains other designations if the source appears in other catalogs. The lists are incomplete due to the diminishing sensitivity of the primary beam towards the edges. The 408 MHz catalog is incomplete for two more reasons. Firstly, the presence of two extended supernova remnants (Joncas, Roger, & Dewdney 1989) prevents the detection of fainter sources within their midst. Secondly, a 20′ wide grating ring crossing the field of view 1 degree south of the field center also hinders detection. It was discovered recently (D. Green 1990, private communication) that the primary beam of one antenna at 408 MHz was shifted to the north/northeast of the phase center of the observations. The short and long baselines are unaffected. Hence the flux densities of the compact sources in the north/northeast were overestimated and those in the south/southwest were underestimated (about 5% for every degree from the phase center). No analysis of the catalog will thus be attempted except for the area within a 30′ radius from the phase center. For this area, the error in flux density due to the phase center shift remains acceptable. Table 5 lists, for the selected area, the sources common to Tables 3 and 4 and the computed 408–1420 spectral index ($S\nu\alpha\nu^{\alpha}$). Five of these sources appear in the Gregory & Taylor (1986) 4760 MHz catalog. Hence 1420–4760 spectral indices were calculated to check on the 408–1420 indices. They do not match exactly. However the number of sources is too small to be able to differentiate between a physical cause (object property) or an inaccurate 408 MHz flux density.

Source 30P75 (31P42, 4C61.02) is the object superposed on Sh 187. It was also observed by Snell & Bally (1986) at 1400 and 5000 MHz with the VLA. They resolved the source in two components. Their total 1400 MHz flux (527 ± 2 mJy) is close to our own. They derived a 1400–5000 spectral index of 1.1, the same as our 408–1420 index. For the faint point source at the northeast boundary of Sh 187 they obtain a 1400 MHz flux density of 10.7 ± 2.8 mJy close to our measurement.

5. H I-LINE OBSERVATIONS

Even though the DRAO synthesis telescope has a 2°.6 field of view and a 105.6 km s^{-1} spectral coverage, we will concentrate

TABLE 5

SPECTRAL INDICES

30P	31P	$\alpha_{408-1420}$	$\alpha_{1420-4760}$
52.....	02	1.4	0.6
55.....	09	0.4	
70.....	35	0.7	0.5
72.....	38	0.5	0.7
75.....	42	1.1	
78.....	46	0.8	
85.....	55	0.9	
87.....	57	0.8	0.9
97.....	72	1.0	
100.....	76	1.1	
103.....	79	1.0	0.6

© American Astronomical Society • Provided by the NASA Astrophysics Data System

1992ApJ...387..591J

our effort on the Sh 187 area. The rest of the field does not contain particular H I features. There is strong galactic plane H I emission from the Perseus arm in the northern part of the field of view ($V_{lsr} < -35$ km s^{-1}) and fainter emission from the nearby Orion arm ($V_{lsr} > -20$ km s^{-1}). Figure 6*b* displays 12 H I maps (line minus out-of-band continuum) of a 50′ field centered on Sh 187. These correspond to adjacent channel maps at full spectral and spatial resolution (see Table 1). Superposed on the maps are two contours of the radio continuum emission from the nebula. The chosen velocity range shows the H I feature most closely related spatially to the H II region. The maps were modified for presentation purposes by having the contribution from the average (over a 50′ diameter patch centered on the field of view) galactic H I line emission subtracted (see Joncas et al. 1985 for an explanation). The average spectrum, encompassing the whole spectral range, is presented in Figure 6*a*. The H I feature takes the form of a thick shell partially surrounding the H II region over the velocity range -12.53 to -19.94 km s^{-1}. Its mean V_{lsr} is -16.2 km s^{-1}, somewhat blueshifted with respect to the velocity of the molecular material. Starting at -12.53 km s^{-1}, the H I emission follows the northwestern contour of the nebula. At more negative velocities, the H I encompasses the H II boundary from east through north and west to south. At about -16.65 km s^{-1} the H I moves behind and/or in front of the nebula, the southeastern boundary being filled at about -18.3 km s^{-1}. Overall the H I emission migrates from the NW to the SE as the velocity becomes more negative. Also apparent (especially at -16.65 km s^{-1}) is the inhomogeneous distribution of matter within the H I region.

Figure 7 is a map showing integrated H I emission over the velocity range -10.06 to -22.42 km s^{-1}. Superposed on the map are a few radio continuum contours from the H II region. The H I "hole" in the southern section corresponds to the location of the background radio source 4C61.02 mentioned above (§§ 4.1 and 4.2). Here the H I is seen in absorption. This map confirms the thick shell-like structure of the H I emission. The lack of H I at the central position where the H II region stands indicates the preponderance of ionized gas and lesser amounts of atomic gas between the object and the observer where the nebula is seen optically. H I self absorption may also be present. The H I emission south of about 61°20′ and west of about 1^h18^m appears mostly at V_{lsr} less than -20 km s^{-1} and thus may not be part of the Sh 187 gas complex.

In order to derive its characteristics, the H I feature was divided in 12 sectors following the same procedure outlined in § 4.1. Table 6 gives for each sector the distance between the peak H I column density ($N_{H\,I}$) and the radio continuum peak, the FWHM and the skewness of the H I profile. If the $N_{H\,I}$ profile has a more extended tail towards the H II region, it is said to be skewed to the interior. These parameters vary from one sector to another but general trends are present. The northeastern section has half the thickness of the rest of the shell with a FWHM of about 2′.5. This area covers about a quarter of the shell; its peak column density is only 1′.5 from the radio continuum peak whereas the other H I peaks are about 3′.5 away. The column density profiles are roughly Gaussian shaped. The mean radius of the H I region is 1.3 pc. This radius was calculated by adding the mean HWHM to the mean distance between the peak H I column density and the radio continuum peak.

The mass of the H I shell depicted in Figure 7 is 70 $M_\odot$. Optically thin conditions were assumed and the H I seen in absorption was accounted for. To learn more about the shell, a three-projection representation of the H I data was produced (Fig. 8). The integrated H I map on the lower left is similar to Figure 7 but covers a smaller area. The shell is clearly clumpy. Three condensations are apparent, they are about 4′ × 3′ in extent and cover 2–3 km s^{-1} along the velocity axis. From the right and upper panel we note that the bulk of the material is at velocities between -15 and -18 km s^{-1}. The peak column densities are at about -17 km s^{-1}. This distribution is definitely blueshifted with respect to the systemic velocity of the complex (-15.0 km s^{-1}). Note the higher proportion of H I in the western half of the shell.

The presence of a strong 1420 MHz point source behind the southern portion of the H I shell is a fortunate coincidence. Figure 9 shows the H I absorption profile. Four of the absorption lines (the most negative at -58.4, -52.0, -42.8, and -37 km s^{-1}) are caused by line-of-sight clouds belonging to the Perseus arm. One line has a positive velocity of 3.4 km s^{-1}. Positive velocities are in principle "forbidden" for this quadrant. However such lines are frequent for the galactic region (Greisen & Lockman 1979). All these lines are fairly narrow

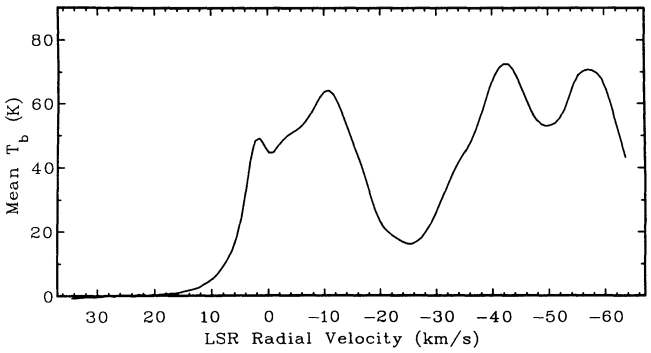

FIG. 6*a*

FIG. 6.—(*a*) "Average spectrum" subtracted from the 128 channel maps of H I emission. The original observed line data in a given channel are obtained by adding the brightness temperature, from the figure, to the proper channel map. This spectrum represents the average H I emission over a 50′ diameter patch centered on Sh 187. (*b*) Maps of H I line emission (minus out-of-band continuum) over a 50′ field centered on Sh 187. All maps are at the full spectral and spatial resolution (see Table 1). The gray levels go from white (<7 K) to black (>37 K). The overlaid contours are continuum emission at 15 and 90 mJy beam^{-1}. The V_{lsr} of each map is indicated at the top of every panel. The beam is depicted in the lower left corner.

TABLE 6

CHARACTERISTICS OF THE H I SHELL

Sector	Peak Radius (pixels)	$N_{H\,I}$ ($\times 10^{21}$ cm^{-2})	FWHM (pixels)	Skewness
1.....	3	2.63	6	exterior
2.....	3	2.15	5	exterior
3.....	3	2.82	5	exterior
4.....	6	2.86	6	interior
5.....	7	2.00	8	interior
6.....	7	1.84	10	none
7.....	point	source		
8.....	point	source		
9.....	7	2.25	9	none
10.....	4	2.44	11	exterior
11.....	5	2.54	8	exterior
12.....	2	2.31	10	exterior

© American Astronomical Society • Provided by the NASA Astrophysics Data System

1992ApJ...387..591J

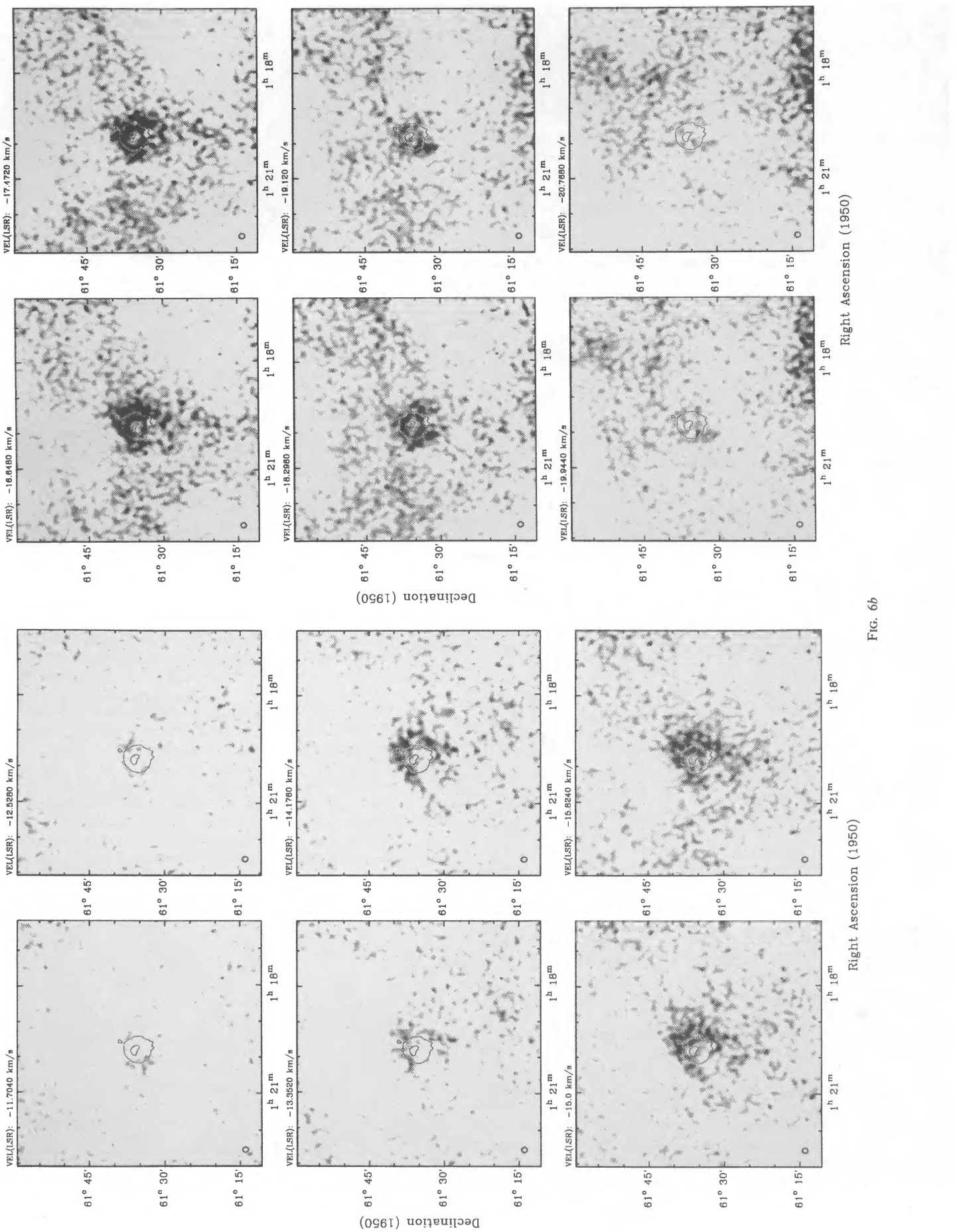

FIG. 6*b*

© American Astronomical Society • Provided by the NASA Astrophysics Data System

1992ApJ...387..591J

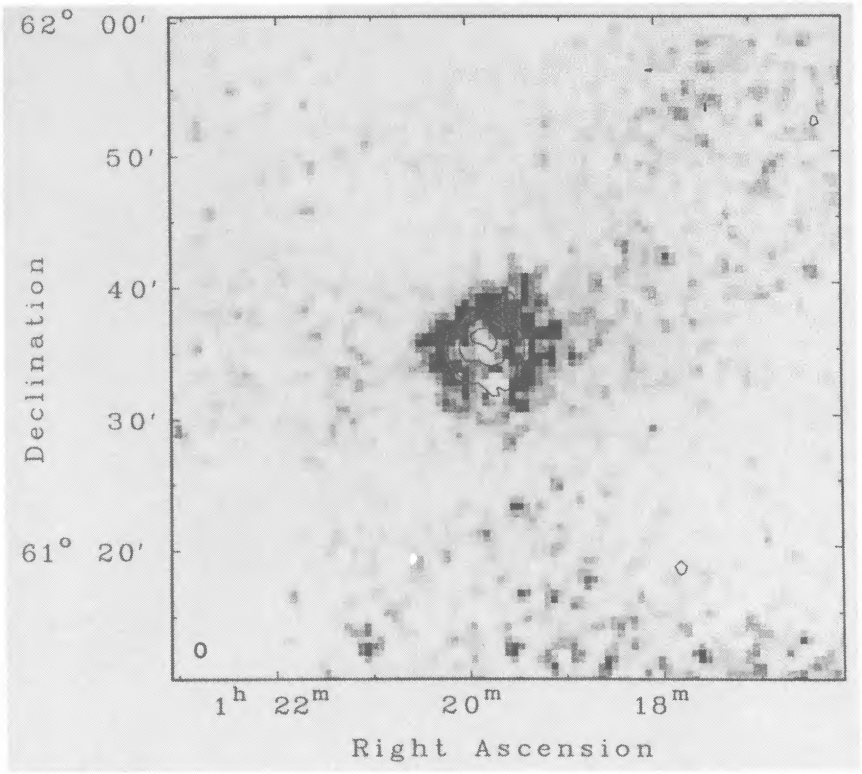

FIG. 7.—Map of integrated H I emission (−10.06 to −22.42 km s^{-1}) in a 50′ × 50′ field centered on Sh 187. The HPBW is shown in the lower left-hand corner. The transitions between the gray levels are at 1, 3, 5, 7, 9, and 11 × 10^{20} cm^{-2}. The overlaid continuum contours are at 15.0, 50.0, 70.0 mJy beam^{-1}. The H I hole present in the southern portion of the H I region is the location of a strong extragalactic radio source where H I is seen in absorption. The peak column density is 3.0 × 10^{21} cm^{-2}.

with a FWHM of about three velocity channels (2.5 km s^{-1}). There is a large absorption line (FWHM of about 5 km s^{-1}) centered at −14.2 km s^{-1} with a peak brightness temperature drop of 20 K. The presence of this absorption line from the H I shell gives us the opportunity to estimate the optical depth (τ) and spin temperature (T_s) of the absorbing gas, assuming T_s is constant in this small portion of the cloud. In the absence of H I emission the following relation can be used

$$T_{ba} = T_{bc} \exp(-\tau) + T_s[1 - \exp(-\tau)] ,$$

where

$$\tau = \tau(\max) \exp(-v^2/2\sigma^2) ,$$

where T_{ba} is the observed brightness temperature drop, T_{bc} is the observed continuum background brightness temperature, v is the central velocity and σ is the standard deviation of the absorption profile. Using the observed quantities yields $\tau = 1.2$ and $T_s = 100$ K. The mean column density of the absorbing gas is estimated to be 1 × 10^{21} cm^{-2}, similar to what was measured from the shell emission profiles.

6. THE MOLECULAR CLOUD

A partial ^{13}CO mapping of the molecular cloud associated with Sh 187 was presented in Joncas et al. (1989). The reader is referred to this paper for details on the observing procedure and the characteristics of the cloud. We reproduce the published map here but this time superposed on the relevant section of the POSS (Fig. 10). The molecular cloud follows closely the morphology of the absorption lane mentioned in § 1. Sh 187 is 1.′5 east of the cloud's core which is almost completely resolved (HPBW = 4.′4) into two components. The molecular outflow and H_2O maser reside in the southern component. At the position of the ^{13}CO emission peak ($1^h20^m21^s$, 61°39′), the line's antenna temperature is 5.4 K, its central V_{lsr} is −15.4 km s^{-1}, and its FWHM is 2.20 km s^{-1}. This corresponds to an H_2 column density of about 2 × 10^{22} cm^{-2}. Assuming a core size of about 0.5 pc, a density of the order of 10^4 H_2 cm^{-3} is present in the center of the molecular cloud. This is in agreement with the detection of NH_3 by Macdonald et al. (1981) at the same position. A close inspection of Figure 7 reveals the presence of a nebulous H I spur extending to the NW of the H I shell. Comparison with Figure 10 shows this spur to coincide in position angle with the molecular cloud. We may be detecting a faint H I envelope surrounding it. We have now completed the ^{13}CO mapping of this cloud which covers 100′ × 80′ (NS × EW) on the sky; these results and high resolution multimolecule mapping of the Sh 187 environment will be the subject of a forthcoming paper (Joncas, Kömpe, & Snell 1991).

7. *IRAS* DATA ANALYSIS

7.1. *Point Sources*

The *IRAS* point source catalog (version 2, 1988) was scanned to identify point sources located within the mapped area of the Sh 187 molecular cloud (Fig. 10). Six sources were found with three valid fluxes (F_λ), 14 with two valid fluxes. All are listed in Table 7, where section A contains the high-quality sources and section B all the other sources. The position of the

© American Astronomical Society • Provided by the NASA Astrophysics Data System

1992ApJ...387..591J

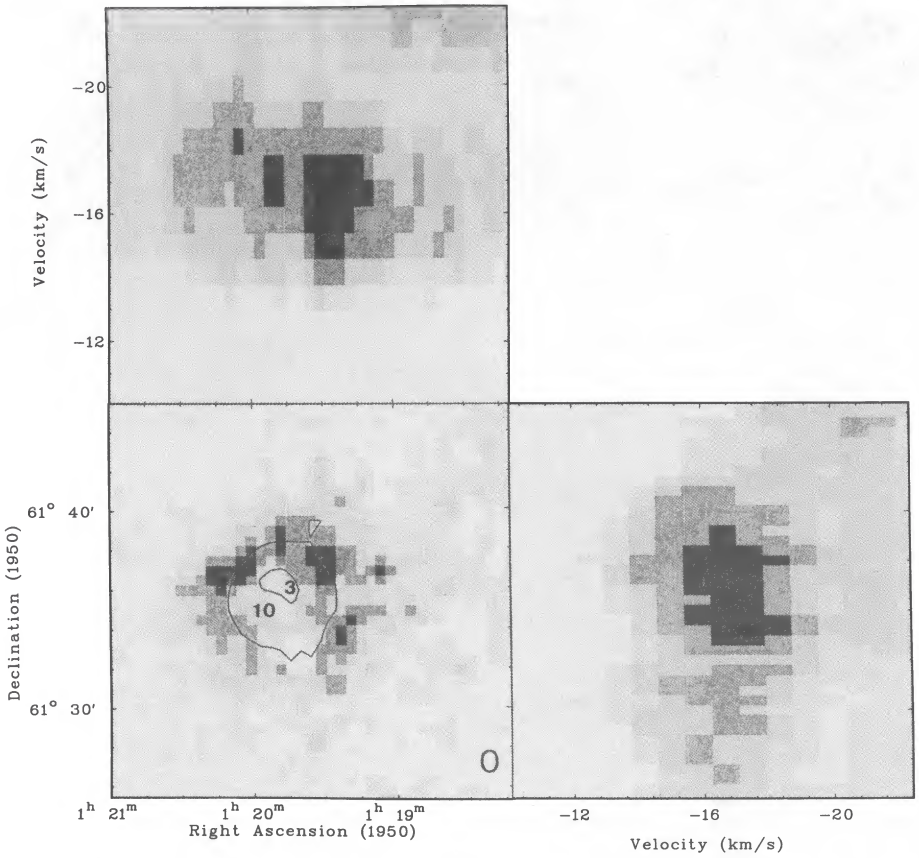

FIG. 8.—Three projection representation of the H I data. Each plot is one face of a R.A.-Decl.-V_{lsr} "cube." The lower left plot is similar to Fig. 8 but is for a 20′ × 20′ field. The overlaid continuum contours mark the position of the H II region at 15 and 50 mJy beam^{-1}. The beam size and shape is indicated in the lower right-hand corner. The position of stars 3 and 10 (see Fig. 1) is also shown. The lower right projection is a Decl.-V_{lsr} plot (i.e., the sum over R.A. of Decl.-V_{lsr} maps). Similarly the upper left panel is a R.A.-V_{lsr} projection.

sources having $F_{12} < F_{25}$ (i.e., nonstellar) is identified in Figure 10 with a designated number indicated in Table 7. The color temperatures (Evans 1980) of the sources are also given in Table 7. Some of the temperatures are lower or upper limits depending on the quality of the measured fluxes.

We will first consider the high-quality sources. Source 2 is located where there is little or no ^{13}CO emission. This may be due to the limited sensitivity of the millimeter observations or the source may not be related to this gas complex. Sources 5 and 3 are projected against the molecular core and the H II region respectively. Both are within the boundaries of the H I shell. Sources 2, 3, and 4 have low $T_{60/100}$ (<23 K), suggesting that they could be dust condensations heated by low-mass stars. The point source catalog also provides the correlation coefficient which is a measure of the extent of the source compared to the profile expected for an ideal point source. According to this coefficient, source 4 deviates by 5% (10% at 100 μm) from a point source giving some credence to the dust condensation hypothesis. J. G. A. Wouterloot (1989, private communication), in a search for H_2O masers associated with *IRAS* sources, observed sources 1 and 6 with the Effelsberg radio telescope. No maser lines were found (rms = 0.06 and 0.07 Jy, respectively). Source 5 is 2′ east of where sits the molecular outflow/H_2O maser combination (§ 1). This separation is 4 times larger than the uncertainty ellipse for its *IRAS* position (26″). Usually all three manifestations are coincident (Wouterloot et al. 1989; Kömpe et al. 1989). The location of source 5 in *IRAS* color-color plots is not inconsistent with its being associated with an H_2O maser (Wouterloot & Walmsley 1986) and molecular outflow (Wouterloot, Henkel, & Walmsley 1989). Source 6 could be a blue planetary nebula according to the color-color plots of Walker et al. (1989) or a T Tauri star following Emerson (1988). We derived the bolometric luminosity for these sources and thus assigned them approximate spectral types using Panagia (1973). We assumed that every

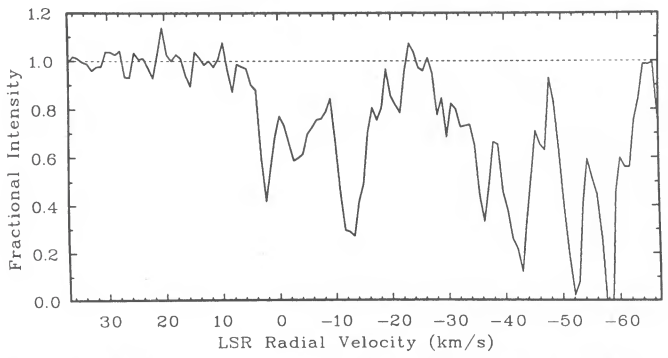

FIG. 9.—H I absorption line spectra at the position of the strong (495 mJy) compact radio source. This spectra is an average over a 6 × 6 pixel area. This spectra covers all 128 velocity channels. The absorption line near −14 km s^{-1} corresponds to the H I region surrounding Sh 187. The lines at more negative velocities are due to H I clouds located in the Perseus arm.

© American Astronomical Society • Provided by the NASA Astrophysics Data System

1992ApJ...387..591J

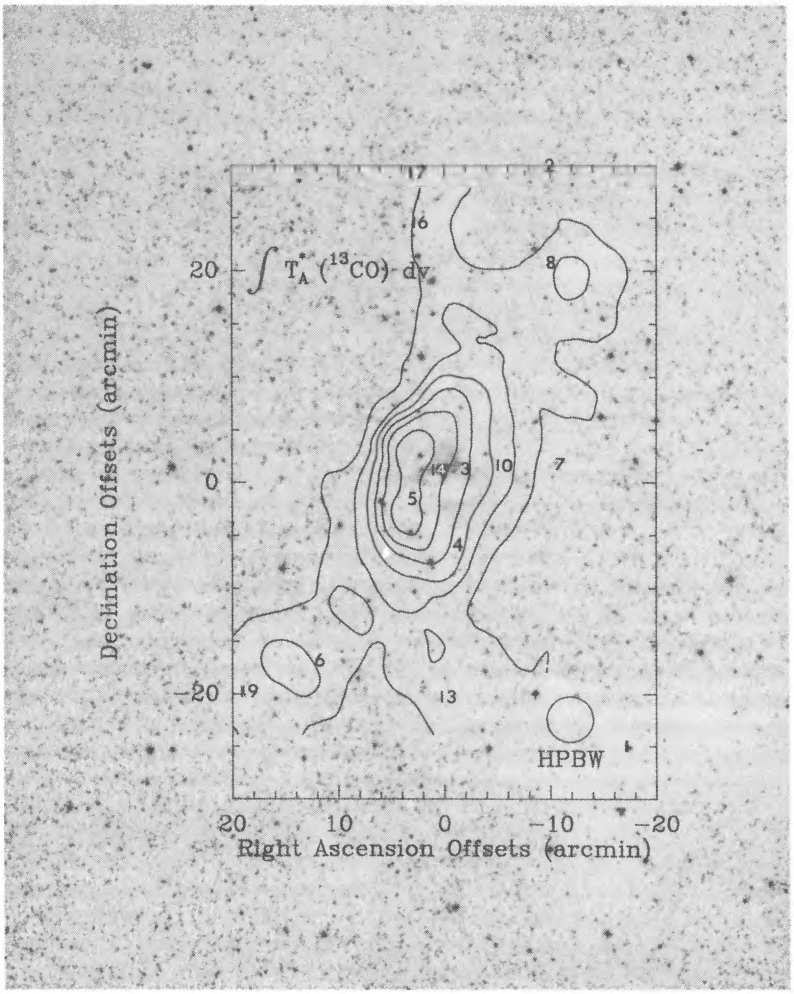

FIG. 10.—Integrated intensity map (−7.0 to −18.0 km s^{-1}) of the ^{13}CO ($J = 1$–0) emission line of part of the Sh 187 molecular cloud. The half-power beamwidth is 4.4, and is shown in the lower right corner. The lowest contour is 2.5 K km s^{-1}, and the contour interval is 2.5 K km s^{-1}. The reference position is $\alpha = 1^h19^m48^s$, $\delta = 61°35'$ (1950 coordinates). The contours are superposed on the relevant region of the Palomar sky survey. The position of the nonstellar *IRAS* point sources are indicated by their designated number (see Table 7).

stellar photon is absorbed by the dust either directly or indirectly. The results are listed in Table 7. No very massive stars were found, all spectral types are later than B2.

Of the sources with two valid fluxes, six have $F_{12} > F_{25} > F_{60}$ indicating that they are probably stars. Source 01224+6120 (no 19) is possibly a T Tauri star as defined by the color-color plots of Beichman et al. (1986) and Walker et al. (1989). According to the latter, source 13 is either a reflection nebula or an H II region. Sources 7, 8, 16, and 17 have low $T_{60/100}$ ($\leq$20 K). Again they could be dust condensations heated by low-mass stars.

The positions of the IR point sources were checked against the location of molecular fragments (Joncas et al. 1991). Practically every point source is located within such a fragment. Source 5 is close to the center of the southern component of the molecular cloud core (−15 to −12 km s^{-1}). Sources 3 and 14 (RAFGL 205) are at the periphery of molecular fragments, and may be related to the H II region (Sh 187) instead of the molecular cloud itself. In fact, source 14 may be a red reflection nebula according to Walker et al. (1989). However, its position coincides (within the error ellipse) with that of star 4 in Figure 1.

At this point we would like to caution the reader. Identifications via color classifications will not always provide unique solutions. This is well illustrated in Emerson (1988).

7.2. *Extended Infrared Emission*

A special *IRAS* data product called survey co-add maps was used for our analysis. The data were obtained through the facilities of the Infrared Processing and Analysis Center (IPAC).[2] These maps are made from a co-adding of the survey scans of the region of interest (see IPAC user's guide) in order to obtain the full angular resolution of the detectors for each band and an increase in sensitivity over the three separate sets of extended emission (HCON) maps. The maps have pixel sizes (sampling) of 15″ at 12 and 25 μm, 30″ at 60 μm, and 60″ at 100 μm. The angular resolutions are 0.76 × 4.45, 0.76 × 4.65, 1.51 × 4.75, and 3.03 × 5.05, respectively.

Prior to 1990, co-added maps required a photometric correction. As a precaution we checked the co-added fluxes of Sh 187 with those derived from the extended emission images

[2] IPAC is funded by NASA as part of the *IRAS* extended mission program under contract to JPL.

© American Astronomical Society • Provided by the NASA Astrophysics Data System

1992ApJ...387..591J

TABLE 7

CHARACTERISTICS OF THE POINT SOURCES

Sources	α(1950)	δ(1950)	$T_{c(12/25)}$ (K)	$T_{c(60/100)}$ (K)	L (10^2 $L_\odot$)	Spectral Type	Comments
			A. High-Quality Sources				
1.....	$1^h17^m30^s$	61°10′35″	107.1	32.5	1.5	<B3	
2.....	1 18 23	62 09 48	<119.5	21.4	0.1	<B3	
3.....	1 19 32	61 36 35	138.3	23.5	25.0	B2	
4.....	1 19 40	61 28 58	135.4	>14.6	2.2	<B3	
5.....	1 20 15	61 33 10	85.9	>25.7	34.0	B2	H_2O maser
6.....	1 21 27	61 18 10	121.7	30.7	2.2	<B3	
			B. Other Sources				
7.....	1 18 15	61 37 22	...	20.1			
8.....	1 18 26	61 55 58	...	17.3			
9.....	1 18 39	61 05 11	176.3	...			star
10.....	1 18 53	61 36 49	122.1	...			
11.....	1 19 26	61 47 25	177.9	...			star
12.....	1 19 45	61 43 59	189.0	...			star
13.....	1 19 51	61 19 49	<120.2	>21.2			
14.....	1 19 51	61 36 23	102.4	...			RAFGL 205
15.....	1 20 06	61 28 24	144.6	...			star
16.....	1 20 12	61 59 35	...	18.4			
17.....	1 20 14	62 08 52	...	19.2			
18.....	1 20 20	61 35 20	150.2	...			star
19.....	1 22 27	61 20 31	<128.9	>17.4			
20.....	1 22 29	61 26 21	165.5	...			star

(Skyflux Plates). Both sets of fluxes agree within 5% (this is a mean value for the four wavelength bands). Advantage was taken of the small extension (about 35′) of the dust emission to use a simple background removal technique. The background was computed via four rectangular areas surrounding the object. The mean value of the IR intensity over the four areas was chosen as the proper background value. The variation from one area to the next was small ($\sigma \leq 0.5$ MJy sr^{-1}). No color correction was applied to the data.

Since co-added maps have pixel sizes varying with wavelength, we chose to present all the emission maps with the same pixel size, 60″. Figures 11*a*–11*d* contain the IR continuum maps of the Sh 187 complex. The first contour is at the 3 σ level. The double peak appearance of the extended emission is in fact caused by the presence of point source 5. The extended emission peak has the same position at every wavelength and it coincides with the 1420 MHz radio continuum peak. The H II region sits at the peak of the IR emission. The objects in the southeastern and southwestern corners are point sources 6 and 1, respectively. The morphology of the IR emission is fairly smooth suggesting the presence of a single heating source and a favorable geometry. The emission seems to favor a NW-SE orientation as for the molecular cloud. The 60 and 100 μm emission maps have a diameter about 10′ larger than the 12 and 25 μm maps. The extension of the 60 and 100 μm emission is almost the same as the part of the ^{13}CO cloud shown in Figure 10. The IR major axis is 10′ shorter while the minor axis is 5′ longer. We know the molecular cloud to be more extended in every direction, hence only part of the cloud receives sufficient heating to produce 100 μm emitting dust. Examination of the 12 and 25 μm intensity maps having a large sampling do not reveal new details about the extended emission.

Table 8 lists the total flux emitted at each wavelength. These were calculated down to the 1 σ level. The area is indicated in Table 8 and extends just a few arcminutes more than the 3 σ level. From these fluxes, a total IR luminosity (8 μm to 2200 μm) was derived to be $2.3 \pm 0.1 \times 10^4$ $L_\odot$ using a νB_ν spectrum. Assuming that the dust grains absorbed every photon emitted by the heating source and reemitted all the energy in the IR, we can derive the spectral type of the source using the computations of Panagia (1973). However, photons are lost to the ISM (see § 4.1), we will thus get a lower limit. A B0 spectral type (ZAMS) was derived assuming that only one star contributes to the heating. The spectral type derived from the radio continuum data is later by about half a spectral class. This difference (which is greater than the uncertainties) suggests the presence of dust mixed with the ionized gas. The later spectral type indicates the absorption of Lyman continuum photons by dust grains. We assume that photon loss to the ISM affects equally both determinations of the spectral type.

The dust color temperatures [T_c(12/25), T_c(25/60), T_c(60/100)] were calculated following the procedure given in Evans (1980). Only the intensities above the 3 σ level were used and the exponent of the emissivity law was taken to be equal to one. These temperatures do not measure a physical grain temperature for reasons which will be explained later in this section. The result of the calculations have been given the form of contour maps (Figs. 12, 13*a*, and 13*b*). The striping is due to the shape of the *IRAS* beams, they are depicted in Figure 11. For T_c(12/25) the 15″ pixel data were used; for the other color temperatures the 60″ resolution was used. The individual color

TABLE 8

INFRARED FLUXES AND AREA OF THE Sh 187 GAS COMPLEX

F(12 μm) (Jy)	F(25 μm) (Jy)	F(60 μm) (Jy)	F(100 μm) (Jy)
365 ± 20	675 ± 90	6700 ± 90	10100 ± 300
758 arcmin^2	800 arcmin^2	1560 arcmin^2	1604 arcmin^2

© American Astronomical Society • Provided by the NASA Astrophysics Data System

1992ApJ...387..591J

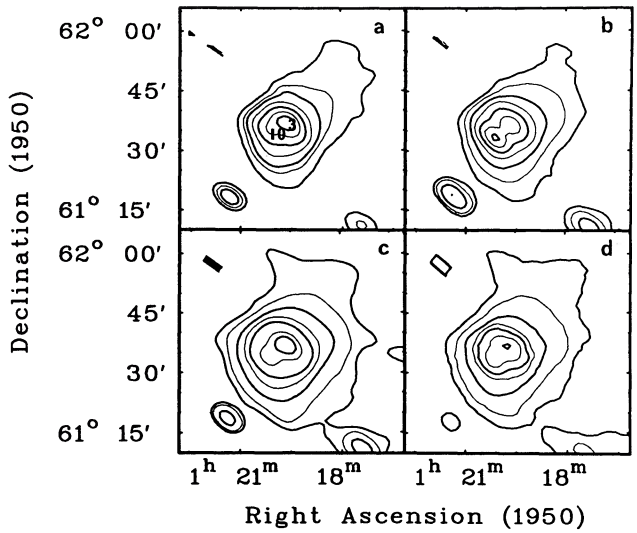

FIG. 11.—(*a*) *IRAS* 12 μm map of the Sh 187 gas complex. The contour levels are at 0.7, 2.2, 4.3, 10.8, 21.6, 36.0, 50.4, and 64.8 MJy sr^{-1}. (*b*) The 25 μm map. The contour levels are at 0.76, 1.9, 5.7, 15.2, 38.0, 76.0, and 123.4 MJy sr^{-1}. (*c*) The 60 μm map. The contour levels are at 1.9, 3.6, 10.8, 36.0, 108.1, 540.7, and 901.2 MJy sr^{-1}. (*d*) The 100 μm map. The contour levels are at 5.6, 14.8, 59.2, 222.0, 444.0, 888.0, and 1480.0 MJy sr^{-1}. All maps have pixel sizes of 1′. The beam shape and orientation is indicated for every wavelength in the upper left-hand corner. The position of stars 3 and 10 (see Fig. 1) is also shown in panel (*a*).

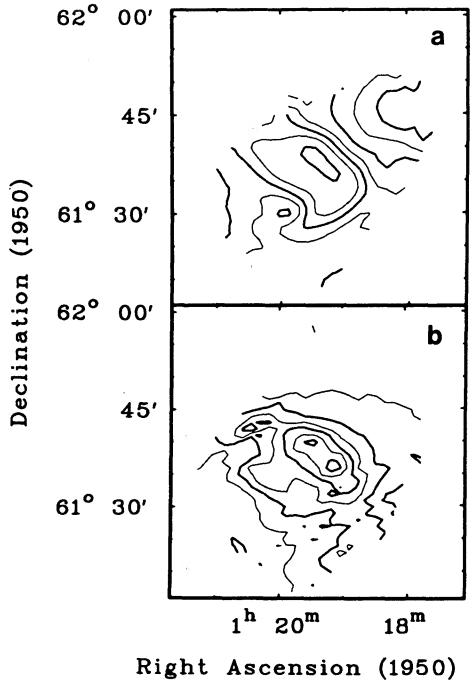

FIG. 13.—(*a*) Contour plot of the dust color temperature, T_c(25/60). The pixel size is 60″. The "peak" contour is at 55 K, the other contours are at 58, 61, 64, 67, 70, and 73 K. The contours are alternatively thick and thin. (*b*) Contour plot of the dust color temperature, T_c(60/100). The pixel size is 60″. The lowest contour is at 26 K (*thick line*), the other contours are at 30, 34, 38, 42, 47, and 52 K (*thick line*).

temperatures have statistical uncertainties of 7% for T_c(12/25) and T_c(25/60), and of 10% for T_c(60/100). However one must keep in mind that the calibration errors are of the order of 30% (Castelaz, Sellgren, & Werner 1987). The mean value of T_c(12/25) is 190 K (1 σ = 21 K, 3988 points). Its minimum value is 115 K and is located at the position of point source 5 and the maximum is 238 K. A secondary minimum is at the position of the H II region. As shown in Figure 12 all large values of T_c(12/25) are at the periphery of the complex away from heat sources. This behavior is at odds with what is expected from a centrally located heating source and the emission mechanism of conventional grains. This phenomenon is now well known if not completely understood. The 8 to 15 μm bandwidth (FWHM) of the *IRAS* 12 μm filter overlaps part of the spectral domain of the "unidentified" IR emission features (7.7, 8.6, 11.3,... μm) (Gillet, Forrest, & Merril 1973) and its associated continuum (Sellgren, Werner, & Dinnerstein 1983) which is described as a 1000 K gray body. The origin of this energy distribution is believed to be transiently heated very small grains (VSG) (see review by Puget & Leger 1989). Hence T_c(12/25) is not a color temperature. T_c(12/25) must be seen instead as a measure of the amount of VSG. (F. X. Desert 1987, private communication). Thus Figure 12 shows that there are less VSG near heating sources than at the periphery of the gas complex. The harsh radiative environment of massive stars either destroys the VSG (Puget, Leger, & Boulanger 1985; Omont 1986) or radiation pressure provokes grain migration.

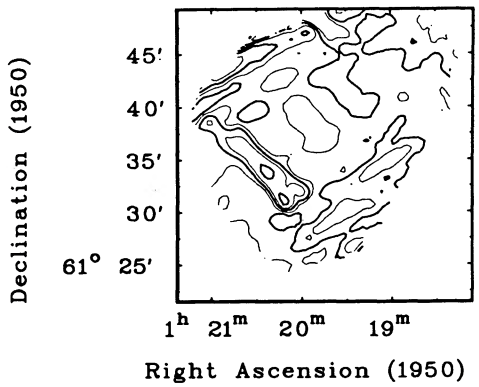

FIG. 12.—Contour plot of the dust color temperature, T_c(12/25). The pixel size is 15″. The lowest contour is at 120 K and is located at ($1^h20^m25^s$, 61°33′). The other contours are at 140, 160, 180, 200, 220 K. The contours are alternatively thick and thin. The higher contours are at the periphery (for example at ($1^h19^m30^s$, 61°28′) T_c = 220 K).

Figure 13*a* shows a contour map of T_c(25/60). Once again the color temperature is lower near the heating sources (point source 5 and the H II region). Actually near source 5 there is a small temperature rise probably caused by the fact that this source is stronger at 25 μm with respect to the rest of the complex than at 60 μm (see Fig. 11*a* and 11*b*). But the T_c(25/60) behavior is somewhat different from T_c(12/25). Starting at the H II region, where T_{min} = 54 K, and going west, T_c(25/60) increases to finally reach 75 K as if we were dealing with VSG. Going east from the H II region, T_c(25/60) increases until source 5; further east T_c(25/60) decreases. This odd behavior may be caused entirely by point source 5 since both cover the same area. Going south T_c(25/60) increases but not as much as for the western side. This is not what one would expect from looking at Figure 12 where there seems to be as much VSG south and west of the H II region. VSG may thus contribute to the emission at 25 μm (actually between 18 and 30 μm the

© American Astronomical Society • Provided by the NASA Astrophysics Data System

1992ApJ...387..591J

filter's FWHM). This was also suggested by Boulanger et al. (1988) in a study of the California nebula. The differences between Figures 12 and 13*a* may result from the 60 μm contribution which originates, at least in part, from conventional grains. Indeed the 60 μm emission may still be contaminated by VSG emission (Ryter, Puget, & Perault 1987; Draine & Anderson 1985). There is also the distinct possibility that another sort of grain is responsible for the 25 μm emission. Cox (1990, and references therein; Duley 1990) suggests this hypothesis as an explanation for the *IRAS* observations of the Rosette nebula. Little is known about the spectral distribution of dust grains at wavelengths longer than 15 μm. This field of study desperately needs spectroscopic information in the 15 to 120 μm range to enlightened our interpretations.

One must also keep in mind that line-of-sight effects, where different dust conditions or composition within the object contribute to what is observed, complicate matters. As an example, note that the peak 12 and 25 μm emission is placed exactly where the H II region is or where VSG cannot survive. Puget et al. (1985) computed that these grains must be further than 5 pc (16'.7 at 1 Kpc) from a B0 star. For the Rosette nebula, Cox (1990) showed the location of the peak 12 μm emission to be right behind the ionization front, in the photodissociation zone of the associated molecular cloud. The Sh 187 VSG emission must then originate from the atomic and molecular material located behind the H II region where they are shielded. The characteristics of the 12 and 25 μm emission can be explained by a combination of two phenomena: the agglomeration of VSG in a high-density environment and the decrease of UV radiation as one goes deeper into molecular material. This is illustrated by the sharp emission decrease seen in the eastern and northern section (Fig. 12*a* and 12*b*) of the gas complex. These are areas of high molecular densities (Joncas, Kömpe, & Snell 1991). To complicate matters even further, let us state that a contribution from hot conventional grains to the 12 and 25 μm emission cannot be rejected (Giard et al. 1989).

Figure 13*b* presents a contour map of $T_c(60/100)$. The maximum value of the color temperature (53 K) is at the position of the principal heating source (the exciting star of the H II region) from where $T_c(60/100)$ decreases in all direction. This is the behavior expected from conventional dust grains. The mean color temperature is 33 K (1 σ = 5 K, 800 points), and the minimum value is 25 K. If VSG do contribute to the 60 μm emission, these values are inaccurate. They are too high if the 100 μm emission is purely thermal. The behavior of $T_c(60/100)$ suggests either that the VSG contribution is relatively small at 60 and 100 μm or that VSG mimic conventional grains at the longer wavelengths. We favor the first hypothesis since conventional grains do contribute in the 60 and 100 μm bands (Greene & Young 1989). Incidentally one may note that the 60 and 100 μm emission cover the same area of the sky and are more extended than the 12 and 25 μm emission.

The mass of the dust emitting at 100 μm can be derived using

$$M_d = (4a\rho/3Q)(\Sigma A_i \tau_i)$$

where a is the grain radius (0.1 μm for conventional grains), ρ is the grain density, Q is the absorption efficiency, τ_i is the 100 μm optical depth at pixel i, and A_i is the area of pixel i. Two things must be kept in mind in using this formula: (1) since a dust temperature is needed to derive τ, $T_c(60/100)$ is used, possibly underestimating τ (see earlier discussion), (2) if very cold dust is present in the molecular cloud it will be missed by *IRAS*, hence preventing M_d being equated to the total dust mass. The quantity M_d was derived to be $1.8 \pm 0.8\ M_\odot$. Using a canonical gas-to-dust ratio of 100, this is less than what one would expect (about 50 $M_\odot$) from the Sh 187 gas complex. The gas mass used is the sum of the ionized, atomic and molecular component. A mass of 4600 $M_\odot$ was used for the molecular cloud (Joncas et al. 1989).

8. DISCUSSION

The Hα velocity field of Sh 187 presented in § 3.3 is rather complicated and we are prevented from suggesting a single scenario. Sh 187 is obviously a young object: its diameter is relatively small (2 pc), a large fraction of the object is still hidden by absorbing material and star formation seems to be going on within the molecular cloud as indicated by the presence of IR point sources, masers, a bipolar outflow and possibly a compact H II region. There are a few phenomena which we expect to be present in a young H II region which has freshly pierced its parental cloud: the expansion of its H II region via a Champagne flow (the result of the pressure discontinuity between the molecular cloud and the intercloud medium when the ionization front broke through to the latter medium), gas flows from either a stellar wind of massive stars or left overs from the bipolar outflow when less massive stars are involved, and finally, flows from dense neutral globules being eroded by the UV flux from the young star(s). The Hα field was measured only over about 3% of the area of the H II region because of intervening absorption. The detected motions occur mainly along our line of sight as suggested by Figure 4. The absence of velocity gradients across the object indicate that the H II region opened up to the intercloud medium directly in front of us. The core's southern fragment illustrates this well: it appears to be squeezed on many sides by neutral material letting ionized gas escape in only one axis (both blue and redshifted material are present) if it contains only ionized material. However the many steep Hα contours (see Fig. 2) can also suggest the presence of ionization fronts (IF), hence of many ionized flows according to current theories. The absence of velocity gradients is thus puzzling unless our limited sampling combined with the geometrical layout of the object prevent us from obtaining a clear picture of its kinematical behavior. Another possibility is that the object is too young to have developed any IF related flows. One-fifth of the measured velocity points have values within 5 km s^{-1} of the systemic velocity of the complex. All we may be seeing is gas escaping from the Stromgren sphere through breaks in the near and far sides of the molecular cloud, in other words a young Champagne flow.

Spitzer (1978) provided relationships describing the expansion of H II regions. Using these one can estimate the dynamical age of an H II region. This value depends on the radius of the initial Stromgren sphere and thus on the density distribution of the neutral material. A nonuniform distribution (which is the case here) may decrease the age since the interclump medium of a molecular cloud has a lesser density (Blitz & Stark 1986). The UV photons will propagate quickly in the interclump medium leaving behind partially ionized globules. However this effect is counterbalanced by the ablation of the globules which fills in the H II region, increasing the density of the interclump gas. Before developing the model further, a verification must be made of the capacity of the globules to produce the measured velocity amplitudes. Bernouilli's theorem for a steady flow gives

$$v^2/2 + c_0^2 \log n = cte\ ,$$

© American Astronomical Society • Provided by the NASA Astrophysics Data System

1992ApJ...387..591J

where v is the ionized gas velocity, c_0 is the sound speed (10 km s^{-1}), and n the density. Comparing the ionized gas's characteristics near (g) and far (f) from the globule we get

$$\frac{n_f}{n_g} = \exp\left[\frac{v_g^2 - v_f^2}{2c_0^2}\right].$$

Taking $v_f = 20$ km s^{-1} and $v_g = 2$ km s^{-1} (the velocity dispersion of the molecular gas), $n_f/n_g = 0.4$. Since the peak density in the H I shell is $\approx 10^3$ cm^{-3} and the peak density of H^+ gas is 100 cm^{-3}, the globules can explain the velocity amplitudes. The presence of many globules will also explain the lack of regular pattern in the velocity field and the line splitting (Dyson 1968). Moreover the globules possess lifetimes similar to the ionizing sources (Tenorio-Tagle 1977). Now let us assume the density of the interclump gas to be equal to the mean density of the molecular cloud (50 cm^{-3}), the dynamical age of the H II region, without allowing for the presence of globules, would be 0.3×10^5 yr. The ablation of the globules will increase the recombination rate hence decreasing the radius of the initial Stromgren sphere. The true age of the H II region will be larger than the dynamical age. To derive the true age, the radio map of Snell & Bally (1986) was used to estimate a mean globule radius and interglobule distance of 1.7×10^{17} cm and 5×10^{17} cm, respectively. The ionized gas will fill in the volume corresponding to half the distance to the nearest globule at a velocity of 15 km s^{-1} (half the measured mean line splitting) in 5×10^3 yr. This time is within a factor of 3 of the time needed to produce an initial Strömgren sphere in a 50 cm^{-3} medium (2×10^3 yr). Using the evaporation rate given by Reipurth (1983), a globule will inject 8.4×10^{55} protons within a volume of 1.7×10^{53} cm^3 in 5×10^3 yr. Hence we will assume that the R-type ionization front producing the Stromgren sphere progressed in a 5×10^2 cm^{-3} medium. The true age of the H II region would then be $\approx 1.8 \times 10^5$ yr.

If the H II region is hidden from view by a dust cloud unrelated to the Sh 187 complex then Spitzer's relations may not apply since the H II region could be totally open to the intercloud medium. The Champagne effect would then dominate. Bodenheimer, Tenorio-Tagle, & Yorke (1979) produced two-dimensional models of such a flow for different geometries. Their case 3, where the exciting star is located in a thin cylindrical cloud, may correspond to what we are observing. The H II region breaks through the molecular cloud in both directions. Maximum velocities of 20 km s^{-1} are calculated after 6×10^4 yr. This time scale is not incompatible with the derived age for Sh 187 since it depends on the clouds thickness. In fact the calculated maximum velocity appears about 5×10^4 yr after the breakthrough. Yorke, Tenorio-Tagle, & Bodenheimer (1984) studied the aspect of spectral lines formed within a Champagne flow. They could produce lines with individual components separated by up to 40 km s^{-1} depending on the specific circumstances and viewing angle. These occurred when globules were involved. Their analysis of case 3 gave a maximum component separation of 18 km s^{-1}. This is less than our mean value of 27 km s^{-1}. Neutral globules must then be kinematically involved in Sh 187. One must not forget that leftover ejections from molecular outflows could also be detected by our observations. Such ejections are known to have velocities in excess of 10 km s^{-1} (Lada 1985). There are no lack of mechanisms to explain the observed velocity field.

Sh 187 is an H II region surrounded by atomic hydrogen and located within a molecular cloud. We interpret the presence of H I as resulting from the dissociation of the molecular material by the processes described in Roger (1983). Dissociated hydrogen zones exist in other star-forming complexes (Roger & Pedlar 1981; Joncas et al. 1985; Dewdney & Roger 1986). These observations prompted the elaboration of a computational model (Roger & Dewdney 1991) which simulates the measurements. Using this model and choosing the parameter values (particularly gas density and stellar type) appropriate to Sh 187, we obtain 1.4 pc for the radius of the dissociation front, 9 $M_\odot$ of ionized hydrogen, and 100 $M_\odot$ of dissociated atomic hydrogen. The predicted values are concordant with an age for the complex of 1.5×10^5 yr.

One expects an expanding IF to be preceded by a thin shocked H I shell as it erodes into a neutral cloud (Spitzer 1978). However, to our knowledge, such a thin shocked shell has not been observed in H I emission. The broader H I zone which partially surrounds Sh 187 is blueshifted with respect to the mean velocity of the molecular cloud and, whether shocked or unshocked, is probably expanding away from the molecular cloud. Even though there is a large difference in the angular resolution between the H I and ^{13}CO data set, we nevertheless compared the LSR velocities "one on one." A blueshift is present across most of the zone. However a comparison of the velocities at the same scale is clearly needed.

Because of its origin the morphology of the H I zone is probably indicative of the characteristics of the molecular cloud. The H I distribution is velocity dependent and is not uniform. We know molecular clouds to be made of condensations (or clumps) surrounded by a less dense interclump medium. This is reflected by the clump nature of the H I region. These may even be partially dissociated clumps analogous to the partially ionized globule discussed earlier. The N-E section of the H I region is thinner than the rest. This section faces the core of the molecular cloud. The presence of denser material is slowing the progress of both the dissociation front and IF. This explanation is supported quantitatively by Roger & Dewdney (1991, their Fig. 9). From the thickness of the H I zone, the "N-E dissociation front" is evolving in a ≈ 1000 cm^{-3} gas density while the "S-W dissociation front" evolves in a ≈ 300 cm^{-3} environment. The H I absorption profile described in § 5 gives physical information on the S-W area of the H I region. Assuming the H I zone to be a thick spherical shell, the H I thickness at the position of the absorption spectra can be calculated. Hence, an H I gas density of 160 cm^{-3} was obtained from a thickness of 2 pc and a mean column density for the absorbing gas of 1×10^{21} cm^{-2} (§ 5), a value concordant with the one predicted. Finally, the H I spin temperature (100 K) derived from the observation can also be compared with the model. Roger & Dewdney (1991) predict a gas temperature of the order of 100 K in the unshocked H I gas.

Infrared point sources and masers can be used to quantify the intensity of the star-forming activity in a gas complex. Five infrared point sources (IRPS) are within the main part of the molecular cloud (Fig. 10). Only one maser was detected which could be related to an IRPS/bipolar outflow. Of the four other IRPS: two may be cold dust condensations, one may be a star with an IR excess, and the last one has the IR colors of sources having a strong 10 μm silicate absorption feature in its spectra (Walker et al. 1989). As listed in Table 7 none of these objects is related to a massive star. We conclude that this gas complex is involved in star forming activity but is not an overflowing nursery. This needs confirmation. Near IR photometry might reveal the presence of numerous enshrouded stars. When our

© American Astronomical Society • Provided by the NASA Astrophysics Data System

1992ApJ...387..591J

molecular observations are fully analyzed, the inproved knowledge of the molecular environment of the detected IRPS will help in establishing their true nature.

The IR and radio data can be usefully combined to give some insights on the physical properties of the dust. It is well-known that the total radio continuum flux at a given frequency is proportional to the number of Lyc photons absorbed per second (N_{rLyc}) by the gas in the H II region. For Sh 187, this number is 1.1×10^{47} photons s^{-1}. From this the number of Lyα photons produced per Lyc photon can be deduced, $N_{Ly\alpha} = AN_{rLyc}$, where A depends on the electron density. For $n_e = 100$ cm^{-3}, $A = 0.67$. From the *IRAS* observations we deduce the total IR luminosity (L_{ir}) of the object (2.3×10^4 $L_\odot$). This luminosity is proportional to the total number of Ly photons emitted per second if we assume that all the energy emitted is absorbed by dust and reradiated in the IR. Thus $L_{ir} = L_{star}$, the stellar luminosity. Hence N_{rLyc} is smaller than $N_{starLyc}$ (Beckman & Norwood 1979). We assume here that the interstellar radiation field (ISRF) does not contribute substantially to the IR luminosity. Boulanger & Perault (1988) have shown that stars earlier than B2 associated to molecular clouds produce luminosities higher than the ISRF. Petrosian, Silk, & Field (1972) have shown that for an H II region

$$L_{ir} = L_{Ly\alpha} + [1 - \exp(-\tau_{Ly})]L_{Lyc} + [1 - \exp(-\tau_{912\,\text{Å}})]L_{912\,\text{Å}},$$

where L_{Lyc} and $L_{912\,Å}$ are the Lyman continuum and below Lyman continuum stellar luminosities, respectively. The τ are the optical depths. Obviously $\exp(-\tau_{Ly}) = N_{rLyc}/N_{starLyc} = 0.48$. According to Panagia (1973), $L_{912\,Å} = 2.34 \times 10^4$ $L_\odot$ and $L_{Lyc} = 1.76 \times 10^3$ $L_\odot$ for a B0 ZAMS star. Since $L_{Ly\alpha} = 3.08 \times 10^2$ $L_\odot$, we obtain that $\tau_{912\,Å} = 2.7$.

So far we have determined $\tau_{100\,\mu m}$ (§ 7) and τ_{Ly}. From these we can determine $Q_{100\,\mu m}$, the dust grain absorption efficiency at 100 μm:

$$Q_{100\,\mu m} = Q_{uv}(\tau_{100\,\mu m}/\tau_{uv}),$$

where $Q_{uv} = 1$ is the ultraviolet absorption efficiency, $\tau_{100\,\mu m}$ is the mean optical depth for Sh 187 at 100 μm, and $\tau_{uv} = \tau_{Ly}$. We get $Q_{100\,\mu m} = 2.7 \times 10^{-4}$. The Kramers-Kronig relation can be used to give a lower limit to the grain size. Assuming the grains to be spherical and using the $Q_{100\,\mu m}$ value obtained earlier a minimum grain size of 40 Å is obtained. One must keep in mind that this value was derived from global properties of the complex.

9. CONCLUSION

A set of multifrequency observations was combined to enable the study of the Sh 187 gas complex. The optical, radio-centimetric, radiomillimetric, and IR observations yielded the following:

1. Star 4 (see Figs. 1 and 2) is possibly the ionizing star of the complex.

2. The optically visible portion of the H II region is fragmented. The presence of steep emission gradients indicates that IF are eroding neutral material.

3. Using Fabry-Perot interferometry, 192 Hα velocity points were measured across Sh 187. The mean V_{lsr} is -17.8 km s^{-1}. Many of the Hα profiles were split in two components. Their mean separation is 30 km s^{-1}.

4. The Hα velocity field is difficult to explain with only one phenomenon: the object possesses either distinct H^+ flows approximately parallel to the line of sight or is subject to some form of Champagne flow.

5. The 1.4 GHz radio continuum map reveals that only about 3% of the H II region is visible optically. Using a distance of 1 kpc for the object and assuming spherical symmetry, we derived that Sh 187 is ionized by a B0.5 star, that its maximum density ($\langle ne \rangle$), averaged over the beam, is 100 cm^{-3}, and that the total mass of ionized gas is 7 $M_\odot$.

6. The H I line observations revealed the presence of an H I feature surrounding part of the H II region. Its mean V_{lsr} is -16.2 km s^{-1}. The H I zone is inhomogeneous and has a varying thickness. Its NE section having half the thickness of the SW section. A H I velocity gradient is also present, the velocities become more negative from the NW to the SE. The mean radius of the H I region (centered on the peak radio continuum emission) is 1.3 pc. The total H I mass is 70 $M_\odot$.

7. A strong compact radio source located behind the H I feature enabled the measurement of an H I absorption spectra. The characteristics of the associated absorbing gas are a V_{lsr} of -14 km s^{-1}, an optical depth of 1.2, and a spin temperature of 100 K.

8. The associated molecular cloud (mean $V_{lsr} = -15$ km s^{-1}) covers more than 1° on the sky. Its core is resolved in two components having densities of the order of 10^4 cm^{-3}. The total mass of the part of the cloud discussed here is ≈ 4600 $M_\odot$.

9. The Sh 187 gas complex contains a number of IR point sources. One may be related to a maser/bipolar outflow. The others are either compact H II regions, heated dust condensations or stars. None have the luminosity expected from a massive (earlier than B) young star.

10. Analysis of *IRAS* co-add maps shows smooth extended IR emission in all bands. The IR emission covers only part of the molecular cloud and is centered on the 1.4 GHz radio continuum peak. The IR luminosity is due to dust grain heating by a B0 star. The dust color temperatures were mapped. The temperature behavior indicates, as expected, that the IR emission originates from at least two different dust populations. The mass of the dust emitting at 100 μm is 1.8 $M_\odot$.

The integration of all these observations was done in § 8. Our principal conclusions are the following:

1. Sh 187 is a fairly young H II region (1–2 $\times 10^5$ yr).

2. The H I region results from the dissociation of the surrounding molecular material. The characteristics of the H I zone (gas density, mass, temperature, radius) are all in good agreement with the predictions of the Roger-Dewdney model of H I dissociation zones around H II regions.

3. Different dust populations exist in star-forming regions. The smallest grains have a radius of 40 Å.

4. The Sh 187 gas complex resides in a "quiet" sector of the local arm with no nearby supernova remnants or OB associations. Will this complex eventually produce massive stars?

We would like to thank the telescope operators of the Observatoire du mont Mégantic and the technical staff of DRAO for all their assistance with these observations. G. J. acknowledges the support of the Natural Sciences and Engineering Research Council of Canada. The Synthesis Telescope of the DRAO is operated as a national facility by the National Research Council of Canada.

© American Astronomical Society • Provided by the NASA Astrophysics Data System

1992ApJ...387..591J

REFERENCES

Baars, J. W. M., Genzel, R., Pauliny-Toth, I. I. K., & Witzel, A. 1977, A&A, 61, 99
Bally, J., & Lada, C. J. 1983, ApJ, 265, 824
Beckman, J. E., & Moorwood, A. F. M. 1979, Rep. Progr. Phys., 42, 87
Beichman, C. A., Myers, P. C., Emerson, J. P., Harris, S., Mathieu, R., Benson, P. J., & Jennings, R. E. 1986, ApJ, 307, 337
Blair, G. N., Peters, W. L., & Vanden Bout, P. A. 1975, ApJ, 200, L161
Blitz, L., & Stark, A. A. 1986, ApJ, 300, L89
Bodenheimer, P., Tenorio-Tagle, G., & Yorke, H. W. 1979, ApJ, 233, 85
Boulanger, F., Beichman, C. A., Desert, F. X., Helou, G., Perault, M., & Ryter, C. 1988, ApJ, 332, 328
Boulanger, F., & Perault, M. 1988, ApJ, 330, 350
Braz, M. A., Scalise, E., Jr., Gregorio Hetem, J. C., Montiero Do Vale, J. L., & Gaylard, M. 1983, A&AS, 77, 465
Castelaz, M. W., Sellgren, K., & Werner, M. W. 1987, ApJ, , 313, 853
Comoretto, G., et al. 1990, A&AS, 84, 179
Cox, P. 1990, A&A, 236, L29
Cox, P., Deharveng, L., & Leene, A. 1990, A&A, 230, 181
Dewdney, P. E., & Roger, R. S. ApJ, 307, 275
Draine, B. T., & Anderson, N. 1985, ApJ, 292, 494
Duley, W. W. 1990, MNRAS, 246, 18p
Dyson, J. E. 1968, Ap&SS, 2, 461
Emerson, J. P. 1988, in Formation and Evolution of Low-Mass Stars, ed. A. K. Dupree & M. T. V. T. Lago (Dordrecht: Kluwer), 193
Evans, II., N. J. 1980, in IAU Symp. 87, Interstellar Molecules, ed. B. Andrew (Dordrecht: Reidel), 1
Fanti, C., Felli, M., Ficarra, A., Salter, C. J., Tofani, G., & Tomasi, P. 1974, A&AS, 16, 43
Felli, M., & Churchwell, E. 1972, A&AS, 5, 369
Felli, M., Churchwell, E., & Massi, M. 1984, A&A, 136, 53
Fich, M. 1986, AJ, 92, 787
Fich, M., & Blitz, L. 1984, ApJ, 279, 125
Georgelin, Y. P. 1970, A&A, 9, 441
Giard, M., Pajot, F., Lamarre, J. M., Serra, G., & Caux, E. 1989, A&A, 215, 92
Gillet, F. C., Forrest, W. J., & Merril, K. M. 1973, AJ, 183, 87
Gower, J. F. R., Scott, P. F., & Wills, D. 1967, MmRAS, 71, 49
Greene, T. P., & Young, E. T. 1989, ApJ, 339, 258
Gregory, P. C., & Taylor, A. R. 1986, AJ, 92, 371
Greisen, E. W., & Lockman, F. J. 1979, ApJ, 228, 740
Haslam, C. G. T., Salter, C. J., Stoffel, H., & Wilson, W. E. 1982, A&AS, 47, 1
Henkel, C., Haschick, A. D., & Gusten, R. 1986, A&A, 165, 197
Higgs, L. A. 1986, JRASC, 80, 51
Israel, F. P. 1977, A&A, 61, 377
Joncas, G., Dewdney, P. E., Higgs, L. A., & Roy, J. R. 1985, ApJ, 298, 596
Joncas, G., Durand, D., Kömpe, C., & Roger, R. S. 1989, in Structure and Dynamics of the Interstellar Medium, ed. G. Tenorio-Tagle, M. Moles, & J. Melnick (Berlin: Springer), 111
Joncas, G., & Higgs, L. A. 1990, A&AS, 82, 113
Joncas, G., Kömpe, C., & De La Noe, J. 1988, ApJ, 332, 1030
Joncas, G., Kömpe, C., & Snell, R. L. 1991, in preparation
Joncas, G., Roger, R. S., & Dewdney, P. E. 1989, A&A, 219, 203
Joncas, G., & Roy, J.-R. 1984, PASP, 96, 263
Kallas, E., & Reich, W. 1980, A&AS, 42, 227
Kassim, N. E., Weiler, K. W., Erickson, W. C., & Wilson, T. L. 1989, ApJ, 338, 152
Kömpe, C., Joncas, G., Baudry, A., & Wouterloot, J. G. A. 1989, A&A, 221, 295
Lada, C. J. 1985, ARA&A, 23, 267
Lo, K. Y., & Burke, B. F. 1973, A&A, 26, 487
Macdonald, G. H., Little, L. T., Brown, A. T., Riley, P. W., Matheson, D. N., & Felli, M. 1981, MNRAS, 195, 387
Mezger, P. G., & Henderson, A. P. 1967, ApJ, 147, 471
Omont, A. 1986, A&A, 164, 159
Panagia, N. 1973, AJ, 78, 929
Puget, J. L., & Leger, A. 1989, ARA&A, 27, 161
Puget, J. L., Leger, A., & Boulanger, F. 1985, A&A, 142, L19
Reipurth, B. 1983, A&A, 117, 183
Roger, R. S. 1983, Proc. Astron. Soc. Australia, 5, 158
Roger, R. S., Costain, C. H., Lacey, J. D., Landecker, T. L., & Bowers, F. K. 1973, Proc. IEEE, 61, 1270
Roger, R. S., & Dewdney, P. E. 1991, ApJ, in press
Roger, R. S., & Pedlar, A. 1981, A&A, 94, 238
Rossano, G. S. 1977, AJ, 82, 587
———. 1978, AJ, 83, 1214
Ryter, C., Puget, J. L., & Perault, M. 1987, A&A, 186, 312
Schraml, J., & Mezger, P. G. 1969, ApJ, 156, 269
Sellgren, K., Werner, M. W., & Dinerstein, H. L. 1983, ApJ, 271, L13
Sharpless, S. 1959, ApJS, 4, 257
Snell, R. L., & Bally, J. 1986, ApJ, 303, 683
Spitzer, L., Jr. 1978, Physical Processes in the Interstellar Medium (New York: Wiley), 254
Stetson, P. B. 1987, PASP, 99, 191
Tenorio-Tagle, G. 1977, A&A, 54, 517
Veidt, B. G., Landecker, T. L., Vaneldik, J. F., Dewdney, P. E., & Routledge, D. 1985, Radio Sci., 20, 1118
Voels, S. A., Bohannan, B., Abott, D. C., & Hummer, D. G. 1989, ApJ, 340, 1073
Walker, H. J., Cohen, M., Volk, K., Wainscoat, R. J., & Schwartz, D. E. 1989, AJ, 98, 2163
Wouterloot, J. G. A., Henkel, C., & Walmsley, C. M. 1989, A&A, 215, 131
Wouterloot, J. G. A., & Walmsley, C. M. 1986, A&A, 168, 237
Williams, D. R. W. 1973, A&AS, 8, 505
Yorke, H. W., Tenorio-Tagle, G., & Bodenheimer, P. 1984, A&A, 138, 325

© American Astronomical Society • Provided by the NASA Astrophysics Data System